Journal of Power Sources 665 (2026) 238956

Contents lists available at ScienceDirect

Journal of Power Sources

journal homepage: www.elsevier.com/locate/jpowsour

Multiscale modelling of supercapacitors with hierarchical structure

Shimeng Qian [a,b], Emily Cheng [a,b,c,d], Odysseas Kakarelidis [a,b], Sang Nguyen [a,b], Milo.S.P. Shaffer [b,c,d], Anthony.R.J. Kucernak [d], Ajit Panesar [a,b,*], Emile S. Greenhalgh [a,b,**]

[a] Department of Aeronautics, Imperial College London, United Kingdom
[b] The Composites Centre, Imperial College London, United Kingdom
[c] Department of Material Science, Imperial College London, United Kingdom
[d] Department of Chemistry, Imperial College London, United Kingdom

HIGHLIGHTS

- A physics-based continuum multiscale model for supercapacitors with hierarchical structure.
- Voltage-dependent double layer capacitance for room-temperature ionic liquid (RTIL) electrolytes.
- Predicted asymmetric capacitance and operating potential window for symmetric porous electrodes in an RTIL electrolyte.

ARTICLE INFO

Keywords:
Supercapacitors
Electrochemical modelling
Porous electrode
Structural electrodes
Ionic liquid
Electric double layer

ABSTRACT

Structural supercapacitors (SSCs) are a class of multifunctional composites that simultaneously provide load-carrying and energy storage capacities. This paper presents a physics-based continuum multiscale electrochemical model aimed at understanding the influence of design decisions on the electrochemical performance of mechanically robust supercapacitors (SCs). The approach was exemplified by considering carbon aerogel-modified carbon fibre-reinforced multifunctional electrodes in a room-temperature ionic liquid (RTIL) electrolyte. The new pseudo 4D (P4D) multiscale model integrates a 3D macroscopic dynamic model to solve the charge transport while coupling a 1D microscopic equilibrium electric double layer (EDL) model to determine the local voltage-dependent double layer capacitance of the porous structural electrode. The numerical model was evaluated to simulate the conventional electrochemical device characterisation methods: cyclic voltammetry, galvanostatic charging and discharging, and electrochemical impedance spectroscopy. The model achieved prediction errors below 10 % for specific energy and capacitance, and around 20 % for specific power. Additionally, an asymmetrical electrochemical behaviour was predicted on the symmetric cell, exhibiting an unbalanced potential window and capacitance at the negative and positive electrodes. Overall, the proposed P4D multiscale electrochemical model provides a powerful tool for analysing, developing, and optimising SSCs and more general SCs with porous electrodes.

1. Introduction

Supercapacitors (SCs) or ultracapacitors have attracted considerable attention in recent years, especially for transportation and renewable energy generation applications, due to the increasing demand for high-power, fast-charging/discharging, long cycle life, and environmentally friendly energy storage devices [1–4]. SCs complement batteries in scenarios where the battery's pulse power capability is exceeded, such as vehicle acceleration, regenerative braking energy recovery and storage, and long lifetime emergency backup systems in electric vehicles [1,3]. Structural supercapacitors (SSCs) [5–7] are a class of multifunctional structural power composites (SPCs) [8] that store electrical energy whilst withstanding significant structural loads. SPCs have the potential to facilitate lightweighting and accelerate the adoption of electrification

* Corresponding author. Department of Aeronautics, Imperial College London, United Kingdom.
** Corresponding author. Department of Aeronautics, Imperial College London, United Kingdom.
E-mail addresses: shimeng.qian21@imperial.ac.uk (S. Qian), e.cheng23@imperial.ac.uk (E. Cheng), o.kakarelidis23@imperial.ac.uk (O. Kakarelidis), snguyen@imperial.ac.uk (S. Nguyen), m.shaffer@imperial.ac.uk (Milo.S.P. Shaffer), anthony@imperial.ac.uk (Anthony.R.J. Kucernak), a.panesar@imperial.ac.uk (A. Panesar), e.greenhalgh@imperial.ac.uk (E.S. Greenhalgh).

https://doi.org/10.1016/j.jpowsour.2025.238956
Received 11 September 2025; Received in revised form 29 October 2025; Accepted 24 November 2025
Available online 3 December 2025

for sustainable transportation. Although SSCs have lower energy density than structural batteries, they are attractive for their long cycle life and volumetric stability in high power applications. The structural abilities of SSCs derive predominantly from the stiff/strong carbon fibre scaffold for the electrodes, supported by a structural electrolyte [9,10] that is sufficiently stiff to provide load transfer across the interfaces between the constituents, with sufficient ionic conductivity for device operation. Conventional supercapacitor/batteries do not offer a structural performance except through the external casing, as the electrodes are based on discontinuous, slurry-cast powders, and the electrolytes are essentially fluids (or weak gels), providing no stress transfer.

The higher specific power density and fast-charging ability of SCs and SSCs are achieved by an electrostatic surface storage mechanism, where the electrolyte ions accumulate within the thin electric double layer (EDL) at the electrode/electrolyte interfaces [11]; capacity correlates with accessible surface area while rates are relatively high since no electron transfer occurs. The performance of the SCs is determined by the material and morphology of the electrodes, in combination with the electrolyte [12]. Plain woven carbon fibres (WCF) are commonly used as the scaffold of the SSC electrodes for their excellent specific mechanical properties and processing stability. However, carbon fibres have a very low specific surface area (SSA) of ~0.2 m^2/g [5] and a low effective roughness factor close to 1, resulting in a low specific capacitance [13]. To increase the SSA of the WCF-reinforced electrode, the carbon fibres can be activated [14], or coated with nanocarbons such as carbon nanotubes [15,16], graphene nanoplatelets [16,17], or carbon aerogels (CAG) [18]; significant increases of the electrode roughness factor (over 7000 in Ref. [18]) can be achieved without appreciably increasing electrode thickness, preserving the volume fraction of structural fillers. In addition, CAG has good mechanical properties (Young's modulus of 23 GPa [19]), improving the load transfer ability between the fibres and thus enhancing the in-plane shear performance of SSC electrodes [7]. The electrolyte is another critical component of SCs since its electrochemical stability window determines the cell operating voltage, and its ionic conductivity plays a vital role in determining equivalent series resistance (ESR) of the cell. The maximum energy and power of SCs increase quadratically with the operating voltage. The typical maximum operating voltage for aqueous electrolytes is about 1.5 V, while for organic electrolytes and ionic liquids (ILs), it can reach above 5 V [20]. Beyond good electrochemical stability, ILs also have high thermal stability, low volatility, low vapour pressure and low flammability, which makes them an attractive selection for SSCs [6,7,9].

The wide range of candidate materials for electrodes and electrolytes in SCs makes experimental exploration laborious; numerical models can significantly reduce the experimental expense in device development and parametric analysis, as well as facilitate the use of digital twins for virtual certification. Physics-based modelling of SCs is challenging due to the multiscale nature of the system (e.g., pores, ion sizes, and double layers are in the nanometre range, electrode and separator thickness are typically tens of micrometres and full device geometries may be in millimetres) as well as the coupled interfacial and transport phenomena that occur across these different length scales [12]. For macroscopic or device-level modelling, equivalent circuit models [21–23] provide an effective means to analyse and interpret the response and performance of SCs under various electrical stimuli. However, this method often struggles to offer any physical insights into the design and optimisation of the electrode morphology or electrolytes. On the other hand, homogenous models [24–26] based on the porous electrode theory (PET) [27] use volume-averaged effective macroscopic properties to describe the dynamic transport phenomenon within the heterogeneous porous electrodes in SCs, for example, treating the double layer capacitance (per unit area) as a constant input. However, this approach ignores the fact that the double layer capacitance is a complex function of the local environment, the electrode material and the type of ionic species that comprise the double layer.

At the micro or nanoscale, Helmholtz [11] introduced the first EDL model analogy to a conventional plane dielectric capacitor, assuming a compact monolayer of counterions forming a second charged layer on a polarised electrode (first charged layer). The EDL plays a fundamental role in determining the specific energy that can be stored in the SCs, where the double layer capacitance (per unit area) of the electrode/electrolyte interface is determined by the potential drop across the EDL and its response to charging [28]. Therefore, understanding and predicting the EDL behaviour in various electrode-electrolyte systems is a vital step. The established Gouy-Chapman-Stern (GCS) model [29–31] works very well for dilute or intermediately concentrated electrolytes on a moderately polarised electrode [28]. However, the accuracy of the GCS model struggles when applied to concentrated electrolytes on a polarised electrode as it does not consider the non-ideality of the species involved, including effects such as ion crowding, steric repulsion and electrostatic correlation effects [32]. To account for these effects, various modified Poisson-Boltzmann (MPB) models [32–34] have been developed based on the mean-field and local-density approximations. Kornyshev et al. [28,35–38] paid particular attention to the EDL behaviour in room temperature ionic liquids (RTILs) and proposed a series of EDL models based on the mean-field lattice gas model. In such ultra-concentrated electrolytes, the ions within the EDL were predicted to obey a "Fermi-like" distribution as opposed to the Boltzmann distribution in the dilute electrolyte. These models capture the asymmetric behaviour of EDL in terms of the differential capacitance and potential distribution during the positive and negative polarisation. Nevertheless, most of the theoretical EDL models discussed above considered planar electrode surfaces, whereas porous electrodes with different microstructures and pore sizes are almost always used in practical energy storage applications. Attempts have been made to extend the classical planar EDL models (generally applicable for macropores over 50 nm) into cylindrical or spherical, and 'slit-shaped' models to capture the significant curvature effects in meso- (2–50 nm) and micro- (<2 nm) pores [39,40], respectively.

Recently, multiscale models of SCs with porous electrodes [21,41,42] that consider both macroscopic dynamic transport within the entire device and microscopic ion adsorption at the EDL have been proposed. However, the microscale modelling for the EDL within these studies either employed the classical GCS model for dilute aqueous electrolytes [21,41] or the MPB model for symmetric concentrated electrolytes [42], with none specifically considering RTILs with asymmetric ionic sizes and their interactions with porous electrodes with different microstructures and pore sizes. Besides, the macroscale models constructed in these models are 1D and assigned with isotropic material properties, which makes them no longer applicable for electrodes with hierarchical structure and anisotropic properties, e.g., CAG-modified WCF-reinforced electrodes in SSCs. SSCs are particularly complex, due to the hierarchical structure of constituents and the pronounced voltage-dependent EDL behaviour in RTIL electrolytes at porous electrodes. To date, there has been no work on modelling supercapacitors with such a configuration.

This study, therefore, proposes a pseudo 4D (P4D) multiscale model to understand the fundamental electrochemical behaviour of SSCs, and SCs more generally, exploiting porous electrodes in RTIL electrolytes. A 3D macroscopic dynamic model for the full cell was established based on the PET and coupled with a pseudo 1D mean-field theory-based equilibrium EDL model for asymmetric ILs in cylindrical mesopores. The numerical model was assigned boundary conditions according to the classical cyclic voltammetry (CV), galvanostatic charge and discharge (GCD), and electrochemical impedance spectroscopy (EIS) experimental tests; the results were compared and validated with experimental data from the previous study by Asfaw et al. [18]. In addition, a range of factors pertinent to the design of both SSCs and general SPCs were studied extensively, including the separator thickness and porosity, electrode thickness and fibre volume fraction. The reported electrochemical model will later be coupled with a mechanical model to develop a fully coupled electrochemical-mechanical modelling

framework for SSCs.

2. Methodology

2.1. Model definition and assumptions

A multiscale modelling framework was established for SC cell devices with hierarchical structure, e.g., SSCs with CAG-WCF electrodes (Fig. 1a), in an RTIL electrolyte (Fig. 1b). The three-dimensional (3D) macroscopic dynamic model considered electrodes composed of cylindrical electrical conductors embedded within a porous, high surface area, electrically conductive matrix, through which an ion conducting electrolyte interpenetrates. The electrodes were separated by a porous electrically insulating separator, which also has an interpenetrating ion-conducting electrolyte passing through it.

Due to the geometric complexity of the electrodes considered, two types of macroscale models were generated, including a 3D full cell (FC) homogenous model and a high-fidelity 3D representative volume element (RVE) model with explicit fibre domains (denoted as 3D-H FC model and 3D-F RVE model, respectively, in Fig. 1b). The 3D-H FC model featured the same geometrical configuration (Fig. S1) as a real 4 $\times$ 4 cm^2 SC pouch cell device and consisted of three main domains: current collector Ω_{CC}, porous electrodes Ω_E^{PC} and separator Ω_{Sep}. The 3D-F RVE model had a cross-sectional area of 50 $\times$ 50 μm^2 and excluded the current collector domain. In this high-fidelity model, the electrode domain $\Omega_E = \Omega_E^{EC} \cup \Omega_E^{PC}$ was further divided into the cylindrical electrical conductor domain Ω_E^{EC} and porous carbon domain Ω_E^{PC}.

The macroscale model was coupled with a pseudo (without physical geometry, elements or nodes) one-dimensional (P1D) microscopic equilibrium cylindrical EDL model (Fig. 1b). The mass and charge conservation were solved within the macroscale model, and the resolved local solid- and liquid-phase potentials were input into the microscale EDL model. The EDL model then determined the local double-layer capacitance and returned it to the macroscale model for solving balance equations in the next time step. The multiscale coupled device-level homogenous and high-fidelity RVE model was denoted as P4D-H FC and P4D-F RVE model, respectively.

The following simplifying assumptions were adopted in the proposed multiscale models.

(1) The porous electrodes were assumed to be ideally polarisable, where no Faradaic current crosses the electrode/electrolyte interfaces.
(2) In the macroscopic model, the EDL was excluded from the quasi-neutral electrolyte region within the porous electrodes [21,41]. The EDL was treated as the source or sink of the net excess counter-ions.
(3) When a certain number of anions/cations were drawn to the EDL, an equal number of cations/anions were repelled from the EDL. Although this assumption may not be valid for the negatively polarised electrodes, for which the charge storage in the EDL was dominated by cation adsorption, rather than the ion exchange mechanism for the positive polarisation charging [43].
(4) The interactions between the ion species were only considered within the thin EDL region and were neglected in the macroscale ion transport modelling [44].
(5) The porous carbon was assumed to exhibit isotropic material properties and a mesopore structure and to fully occupy the void region of the electrical conductor scaffold.

2.2. Governing equations

The porous electrodes were considered as the superposition of two continuous phases, i.e., a solid conducting porous carbon phase and a pore-filling liquid IL electrolyte phase, at any point in the domain $\boldsymbol{x} \in \Omega_E^{PC}$ (Fig. 1b). Volume-averaged variables and parameters over the pores were utilised in this model, without considering the actual geometric details of the pores. Three main time-continuous variables were solved in the time interval $t \in [0, t_{end}]$, including the solid-phase potential $\phi_s(\boldsymbol{x}, t)$ in the porous electrodes domain $\boldsymbol{x} \in \Omega_E^{PC}$, the liquid-phase

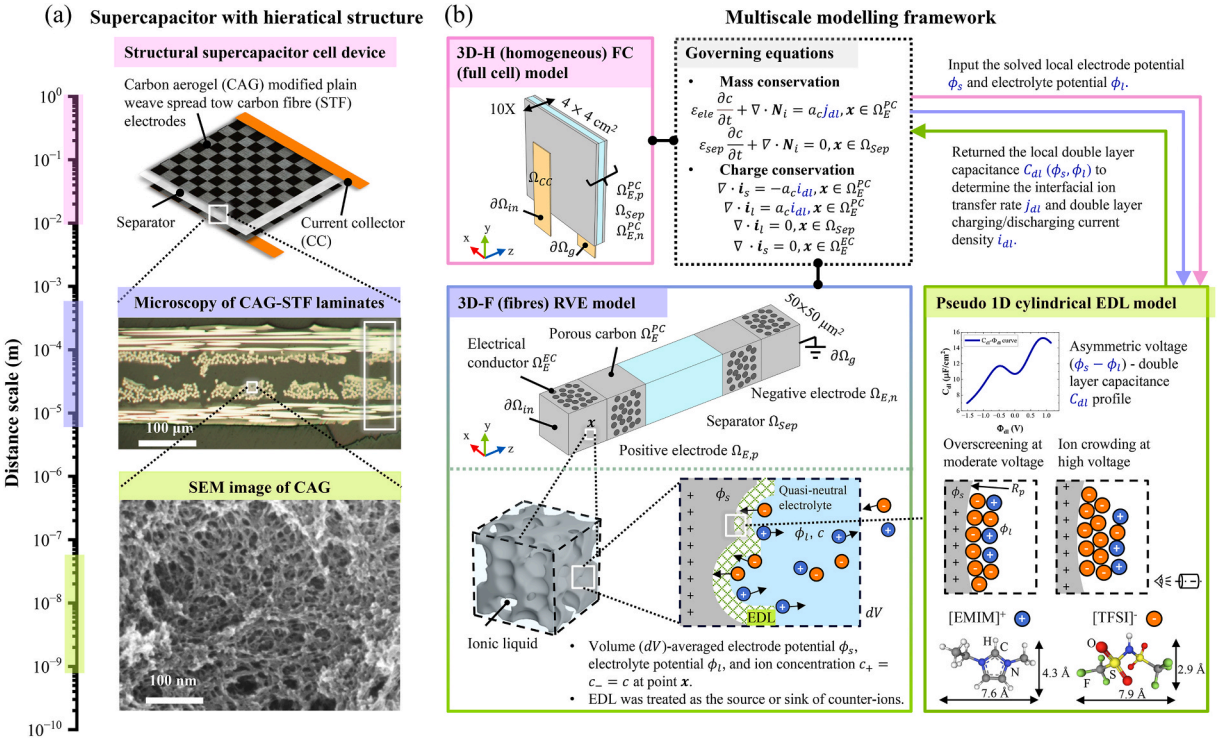

Fig. 1. (a) Illustration of a laminated SSC cell device as a case of SCs with hierarchical structure; (b) a multiscale modelling framework that couples a 3D macroscopic full cell or RVE model with a pseudo 1D microscopic cylindrical EDL model.

potential $\phi_l(\boldsymbol{x},t)$ and ion molar concentration $c_i(\boldsymbol{x},t)$ ($i = +, -$, referring to cation and anion, respectively) over the entire porous electrodes (pore-volume averaged) and the separator domain $\boldsymbol{x} \in \Omega_E^{PC} \cup \Omega_{Sep}$. Given the electroneutrality assumption, the molar concentration of the cations and anions was equal in the pore-electrolyte (outside of the EDL) and bulk, i.e., $c_+ = c_- = c$.

The mass conservation of ions in the liquid phase of the porous electrodes follows:

$$\varepsilon_{ele}\frac{\partial c}{\partial t} + \nabla\cdot\boldsymbol{N}_i = a_c j_{dl}, \boldsymbol{x} \in \Omega_E^{PC} \tag{1}$$

where ε_{ele} is the average porosity, $a_c = A_c a_s$ is the electrolyte accessible specific surface area (SSA) per unit volume of the electrode, A_c is the electrolyte accessibility, and a_s is the theoretical maximum SSA of the porous electrode obtained using the Brunauer-Emmett-Teller (BET) test. $\boldsymbol{N}_i$ is the mass flux density averaged over the cross-sectional area of the electrode, describing the average number of moles of species i moving per unit time (i.e., average velocity $\boldsymbol{v}_i$) across a plane of 1 m^2. The divergence of $\boldsymbol{N}_i$ determines the species at the point $\boldsymbol{x}$ to move towards (if $\nabla\cdot\boldsymbol{N}_i < 0$) or away (if $\nabla\cdot\boldsymbol{N}_i > 0$) from that point. j_{dl} is the pore-wall flux density averaged over the solid-liquid interfacial area, which is the normal component of the ion flux density at the pore wall, representing the number of moles of ions moving from the solid to liquid phase of pores per unit time per unit interfacial area, i.e., interfacial ion transfer rate per unit surface area. The pore-wall flux can stem from Faradaic processes, capacitive processes, or a combination of both ($j_{in} = j_{faradaic} + j_{dl}$). In this study, Faradaic processes were not considered (assumption (1)), thereby, the pore-wall flux density only accounts for the EDL charging/discharging flux density j_{dl}. Therefore, $A_c a_s j_{dl}$ describes the ion transfer rate (per unit volume) within the EDL region, from the solid to liquid phase ($j_{dl} > 0$) or vice versa ($j_{dl} < 0$) [27]. That is, double layer charging/discharging on the pore surfaces was considered as a volumetric source/sink term in the macroscopic volume-averaged transport equation [21,24,42].

The charge conservation within the porous electrode domain gives:

$$\nabla\cdot\boldsymbol{i}_s = -a_c i_{dl}, \boldsymbol{x} \in \Omega_E^{PC} \tag{2}$$

$$\nabla\cdot\boldsymbol{i}_l = a_c i_{dl}, \boldsymbol{x} \in \Omega_E^{PC} \tag{3}$$

where $\boldsymbol{i}_s$ and $\boldsymbol{i}_l$ are the electronic and ionic current densities, respectively. i_{dl} is the average EDL charging/discharging current density (positive in the direction from the solid to the liquid phase). The divergence of the total current equals zero (i.e., $\nabla\cdot(\boldsymbol{i}_s + \boldsymbol{i}_l) = 0$), resulting from the electroneutrality assumption [27].

Similarly, the mass and charge conservation for the bulk electrolyte within the separator domain are expressed as:

$$\varepsilon_{sep}\frac{\partial c}{\partial t} + \nabla\cdot\boldsymbol{N}_i = 0, \boldsymbol{x} \in \Omega_{Sep} \tag{4}$$

$$\nabla\cdot\boldsymbol{i}_l = 0, \boldsymbol{x} \in \Omega_{Sep} \tag{5}$$

where ε_{sep} is the porosity of the separator. Since the separator is electrically insulating, no electronic current flows within it.

In the case where carbon fibre domains were explicitly constructed, fibres were treated as charge conductors with charge conservation, which yields:

$$\nabla\cdot\boldsymbol{i}_s = 0, \boldsymbol{x} \in \Omega_E^{CF} \tag{6}$$

2.3. Constitutive law

The mass flux density $\boldsymbol{N}_i$ in the mass balance equation (1) was described by the Nernst-Planck equation, where the movement of the species i at a point $\boldsymbol{x}$ with a velocity $\boldsymbol{v}_i$ is driven by both the concentration gradient ∇c_i and potential gradient in the electrolyte $\nabla\phi_l$ as:

$$\boldsymbol{N}_i = c\boldsymbol{v}_i = -D_i^{eff}\left(\nabla c - z_i\frac{F}{RT}c\nabla\phi_l\right) \tag{7}$$

where $z_+ = -z_- = 1$ is the number of electronic charges carried by an ion i, F is the Faraday's constant, R is the universal gas constant, and T is the absolute temperature. Any interactions between the ions during the ion transport are neglected in this model. The effective diffusion coefficient D_i^{eff} of species i in a porous medium is determined by the porosity ε_m and the tortuosity factor τ_m of the medium, and the bulk diffusion coefficient D_i^{bulk}, following:

$$D_i^{eff} = \frac{\varepsilon_m}{\tau_m}D_i^{bulk} \tag{8}$$

where $m = ele, sep$ refers to the porous electrode and separator, respectively. Based on Bruggeman's model, the porosity-tortuosity relationship follows $\tau_m = 2\varepsilon_m{}^{-1/n}$, where $n = 2$ for spherical obstructions (for $m = ele$, applied for porous CAG electrodes) and $n = 1$ for cylindrical obstructions (for $m = sep$, applied for separators with fibre type reinforcements) [45]. A factor of two was applied to mitigate the underestimation issue when using Bruggeman estimation for the battery electrodes and separators [46]. The current density in the electrolyte $\boldsymbol{i}_l$ is defined in terms of the ion flux by:

$$\boldsymbol{i}_l = F\sum_i z_i\boldsymbol{N}_i \tag{9}$$

Simply, the current density in the solid phase of the electrodes $\boldsymbol{i}_s$ follows Ohm's law as:

$$\boldsymbol{i}_s = -\boldsymbol{\sigma}_s\nabla\phi_s \tag{10}$$

where $\boldsymbol{\sigma}_s$ is the electrical conductivity of the solid electrode.

The double layer (pore-wall) flux j_{dl} in the phenomenological source/sink term in the equation (1) is calculated from the double layer charging/discharging current density i_{dl}, following [24]:

$$z_i F j_{dl} = -\frac{dq_i}{dq}i_{dl} \tag{11}$$

$$i_{dl} = \frac{\partial q}{\partial t} = C_{dl}\frac{\partial(\phi_s - \phi_l)}{\partial t} \tag{12}$$

where $z_i F$ is the charge per mole on a species i, $dq_+/dq = dq_-/dq = -0.5$ indicates an equal contribution of cation and anion on the change of the surface charge q on the EDL.

The differential double layer areal capacitance $C_{dl} = \partial q/\partial(\phi_s - \phi_l) = C_{dl,c}^{GK}$ (in F/m^2) for porous CAG in IL was predicted by the Kornyshev-Goodwin model [37,38] based on the mean-field theory with further modifications accounting for the pore curvature effect based on the electric double-cylinder capacitor model (Fig. 1b) in Ref. [39] for mesopores (2–50 nm). The correlation between the double-planer capacitance $C_{dl,p}^{GK}$ and double-cylinder capacitance $C_{dl,c}^{GK}$ follows:

$$C_{dl,c}^{GK} = \frac{d}{R_p\ln\left(R_p/(R_p - d)\right)}C_{dl,p}^{GK} \tag{13}$$

where R_p is the average radius of the CAG pores, $d \approx a_i/2$ is the distance between the pore wall and the centre of the ion i (with ion size of a_i), and $C_{dl,p}^{GK}$ is given by:

$$C_{dl,p}^{GK} = \widetilde{C_0}\frac{cosh\left(\frac{\alpha u}{2}\right)}{1 + 2\gamma\, sinh^2\left(\frac{\alpha u}{2}\right)}\sqrt{\frac{2\gamma\, sinh^2\left(\frac{\alpha u}{2}\right)}{ln\left(1 + 2\gamma\, sinh^2\left(\frac{\alpha u}{2}\right)\right)}} \tag{14}$$

$$\gamma = \gamma_- + \frac{\gamma_+ - \gamma_-}{1 + exp\left(\frac{\alpha u}{2}\right)} \tag{15}$$

$$u = \frac{\phi_s - \phi_l}{\phi_T} = \frac{F(\phi_s - \phi_l)}{RT} \tag{16}$$

where $\widetilde{C_0} = \sqrt{\alpha}C_0$ is the Debye capacitance with the rescaling factor $\alpha < 1$ accounting for the short-range ion correlations. u is the dimensionless potential drop across the EDL, normalised by the thermal potential $\phi_T = RT/F = 26$ mV. $\gamma < 1$ is the ion compacity parameter, presenting the average number of ions in the bulk to the maximum capacity of ions in a mean-field lattice-gas model [35,36], and γ_+ and γ_- are the ion fractions of cations and anions, respectively.

2.4. Electronic perturbation boundary conditions and initial conditions

Zero mass flux and electrical insulated boundary conditions were applied on the entire exterior surfaces $\partial\Omega_{ext}$ of the cell RVE (Fig. 1b):

$$-\vec{\boldsymbol{n}} \cdot \boldsymbol{N}_i = 0, -\vec{\boldsymbol{n}} \cdot \boldsymbol{i}_l = 0, -\vec{\boldsymbol{n}} \cdot \boldsymbol{i}_s = 0, \boldsymbol{x} \in \partial\Omega_{ext} \tag{17}$$

where $\vec{\boldsymbol{n}}$ is the outward unit normal vector on $\partial\Omega_{ext}$.

The outer surface of the negative electrode perpendicular to the thickness direction was connected to the electrical ground, which gives:

$$\phi_s = 0, \boldsymbol{x} \in \partial\Omega_g \tag{18}$$

The corresponding outer surface on the positive electrode was connected to the input signal according to the electrochemical test performed by setting.

- Galvanostatic charge and discharge (GCD) test

$$\iint \boldsymbol{i}_s \cdot \boldsymbol{n} dS = I_{GCD}(t) \tag{19}$$

where dS is the surface boundary where the electronic perturbation was applied, $I_{GCD}(t)$ is the input cell charging/discharging current defined as:

$$I_{GCD}(t) = \begin{cases} I_{ch}, & for\ 2(n-1)\tau_{GCD} \le t < (2n-1)\tau_{GCD} \\ -I_{ch}, & for\ (2n-1)\tau_{GCD} \le t < 2n\tau_{GCD} \end{cases}, \boldsymbol{x} \in \partial\Omega_{in} \tag{20}$$

where I_{ch} is the input charging current, n is the cycle number, τ_{GCD} is the cycle period accounting for the time to charge to the operating cell voltage V_O and then discharge to the minimum cell voltage V_{min}.

- Cyclic voltammetry (CV) test

$$\phi_s = \phi_{CV}(t), \boldsymbol{x} \in \partial\Omega_{in} \tag{21}$$

where $\phi_{CV}(t)$ is the prescribed potential varied linearly with time according to:

$$\phi_{CV}(t) = \begin{cases} V_{min} + \nu t, & for\ 2(n-1)\tau_{CV} \le t < (2n-1)\tau_{CV} \\ V_{max} - \nu[t - (2n-1)]\tau_{CV}, & for\ (2n-1)\tau_{CV} \le t < 2n\tau_{CV} \end{cases} \tag{22}$$

where ν is the scan rate, $\tau_{CV} = 2(V_{max} - V_{min})/\nu$ is the cycling period.

- Electrochemical impedance spectroscopy (EIS) test

$$\phi_s = \phi_{EIS}(t), \boldsymbol{x} \in \partial\Omega_{in} \tag{23}$$

where the imposed electric potential $\phi_{EIS}(t)$ consists of a direct current (DC) potential ϕ_{dc} and a sinusoidal oscillating potential with a small amplitude ϕ_o, written in complex notation as:

$$\phi_{EIS}(t) = \phi_{dc} + \phi_o e^{i2\pi ft} \tag{24}$$

where f is the frequency.

The initial conditions for the solid electrode and electrolyte potential, as well as the electrolyte concentration are given:

$$\phi_s = \phi_{s0}, \boldsymbol{x} \in \Omega_E^P, t = 0 \tag{25}$$

$$\phi_l = \phi_{l0}, \boldsymbol{x} \in \Omega_E^P \cup \Omega_{Sep}, t = 0 \tag{26}$$

$$c = c_{bulk}, \boldsymbol{x} \in \Omega_E^P \cup \Omega_{Sep}, t = 0 \tag{27}$$

where c_{bulk} is the bulk concentration of the IL electrolyte.

3. Finite element (FE) implementation and model validation

3.1. FE implementation

The model was implemented within COMSOL Multiphysics 6.2, using the Tertiary Current Distribution, Nernst-Planck interface with the electroneutrality charge conservation option and solved with a time-dependent solver. The 3D and 1D macroscopic models were discretised by quadratic tetrahedral elements and quadratic edge elements, respectively. The input physics constants and material parameters are summarised in Table A.3. In the high-fidelity RVE model, the actual material properties of the electrically conductive scaffold and the porous carbon were assigned to the corresponding domains separately. In the macroscopic homogeneous FC model (Fig. 1b), the effective homogenised properties of the entire electrodes were assigned to the porous electrode domain. Mesh convergence studies were conducted for each of the numerical models established in this study to ensure mesh independence of the finite element results.

3.2. Model validation

The proposed electrochemical model was validated by comparing the numerical results with the experimental results of an SSC pouch cell with a liquid electrolyte [18] which had undergone a series of electrochemical tests, including CV, GCD and EIS. The pouch cells consisted of a pair of CAG-modified plain weave spread tow carbon fibre fabrics (STFs). The parent fabric was TeXtreme 43 PW HS40 12 K, Oxeon AB, Sweden, and the CAG loading was 22 wt%; the detailed manufacturing process for this structural electrode was reported in Ref. [18]. The electrodes were 4×4 cm^2 in size and 107 ± 4 μm thick, with a total mass of 179 mg for a pair. These electrodes sandwiched a non-woven glass fibre fabric separator (Optiveil® E-glass 20103A, Technical Fibre Products), which was 6×6 cm^2 and 240 μm thick. A graphite strip was placed on the outer surface of the CAG-STF electrodes as the current collector and the assembly was then infused with 2–5 mL 1-ethyl-3-methylimidazolium bis(trifluoromethylsulfonyl)imide ([EMIM][TFSI], >98 %, Sigma Aldrich) ionic liquid electrolyte (see ESI for detailed geometrical configurations).

The performance of the cell model was evaluated according to several critical metrics, including the equivalent series resistance (ESR) R_{ESR}, specific capacitance C_s, time constant τ, specific energy Γ_s and power P_s (see ESI for detailed calculation methodology). The gravimetrical performance indices of a cell device were normalised by the mass of the two structural electrodes to be comparable with the experimental data in Ref. [18], according to the protocol of reporting the performance of SPCs [47].

4. Results

The numerical results of conducting CV, GCD and EIS simulations on the full cell homogenous models presented in this work were delivered and compared with the previous experimental results [18]. In GCD simulations, which aim to predict cell performance in a practical context, the P4D-H FC model featuring the same geometrical configuration as the real pouch cell (Fig. S1) was employed, while other electrochemical test simulations and subsequent parametric studies were performed with the P2D-H FC model.

4.1. Cyclic voltammetry (CV)

The numerical model replicated the rectangular-shaped cyclic voltammograms characteristic of real supercapacitors, with a distortion associated with internal resistance increasing as the scan rate increased from 5 to 200 mV/s (Fig. 2a and b). A lower level of resistive distortion was observed in the numerical curves at varying scan rates compared to the corresponding experimental results. Furthermore, the slight redox peak near the maximum voltage in the experimental curve of 5 mV/s was not captured by the models.

With an increasing scan rate v, the response current i at a particular cell voltage was predicted to increase linearly, whereas a non-linear response was observed in the experimental i-v profile (Fig. 2c). Similarly, the specific capacitance C_s predicted by the numerical model decreased linearly with increasing scan rate. In contrast, the experimentally measured C_s showed a more rapid decline at low scan rates, followed by a more gradual, near-linear decrease at higher scan rates (Fig. 2f). Besides, the maximum specific capacitance obtained from the numerical simulation ($C_s^{num} = 4.5$ F/g at 5 mV/s) was underpredicted by 9.5 % compared to the experimental result ($C_s^{exp} = 5.0$ F/g at 5 mV/s).

Additionally, the specific capacitance of the positive electrode ($C_{s,p}^{num} = 19.6$ F/g at 5 mV/s) was predicted to be over 10 % higher than that of the negative electrode ($C_{s,n}^{num} = 16.5$ F/g at 5 mV/s) (Fig. 2f). As a result, the potential window of the negative electrode ($\Delta V_n = 1.09$ V at 5 mV/s) was inversely higher than that of the positive electrode ($\Delta V_p = 0.91$ V at 5 mV/s) to maintain the charge balance (Fig. 2d and e). With the increase of the scan rate, the electrode asymmetry tended to decrease, with the difference in specific capacitance at the two electrodes reduced from around 16 % to just over 10 % (Fig. 2f).

4.2. Galvanostatic charge and discharge (GCD)

The predicted GCD curves (solid lines) of the P4D-H FC model for a two-electrode symmetrical supercapacitor system replicated the typical SC-like response observed experimentally (dotted curves) [18], showing a symmetric triangular-shaped voltage-time profile during varying constant current charging and discharging processes (Fig. 3a). A slight deviation from the linear voltage-time relationship for the modelled SCs was observed in the numerical curves. A more pronounced nonlinear response was observed in the experimental devices, where the GCD curves started to level off at higher potentials during charging, especially at small current densities (e.g., 0.625 mA/cm^2, or 10 mA/16 cm^2, Fig. 3a). The ohmic drop (IR drop) at the transition of charging and discharging was predicted to increase linearly with increasing current density, giving an ESR of 2.1 Ω (34 Ω cm^2) and 2.7 Ω (43 Ω cm^2) for P2D-H FC and P4D-H FC models, respectively, about 20 % and 40 % lower than that of the experimental value of 3.6 Ω (58 Ω cm^2) (Fig. 3b).

The Ragone plot (Fig. 3c) summarises the specific energy and power of both P2D-HFC and P4D-H FC models undergoing GCD at varying current density from 0.125 to 18.75 mA/cm^2. A constant electrolyte accessibility A_c was initially assumed in the numerical models, and the value of 0.31 was calibrated based on the experimental CV curve at 5 mV/s (see ESI for detailed calibration procedure). At the lower current densities (0.125–1.25 mA/cm^2, or 2–20 mA/16 cm^2), a generally acceptable error of less than 30 % was obtained between the numerical and experimental results in both specific energy and power for both models (Fig. 3c). However, at higher current densities (over 6.25 mA/cm^2, or 100 mA/16 cm^2), the tendency to overestimate the specific energy became more pronounced, which associated with the over-predicted specific capacitance (Fig. 3d). As the charging rate decreased, both simulation and experimental data exhibited an approximately linear increase in specific capacitance at elevated current densities. While the experimental device demonstrated a more abrupt capacitance boost when the charging rate was reduced to the lower current density range, eventually reaching a maximum cell specific capacitance of 2.6 F/g at 0.125 mA/cm^2, about 20 % higher than the corresponding numerical value of 2.1 F/g.

To explore the effects of electrolyte accessibility on the overall cell

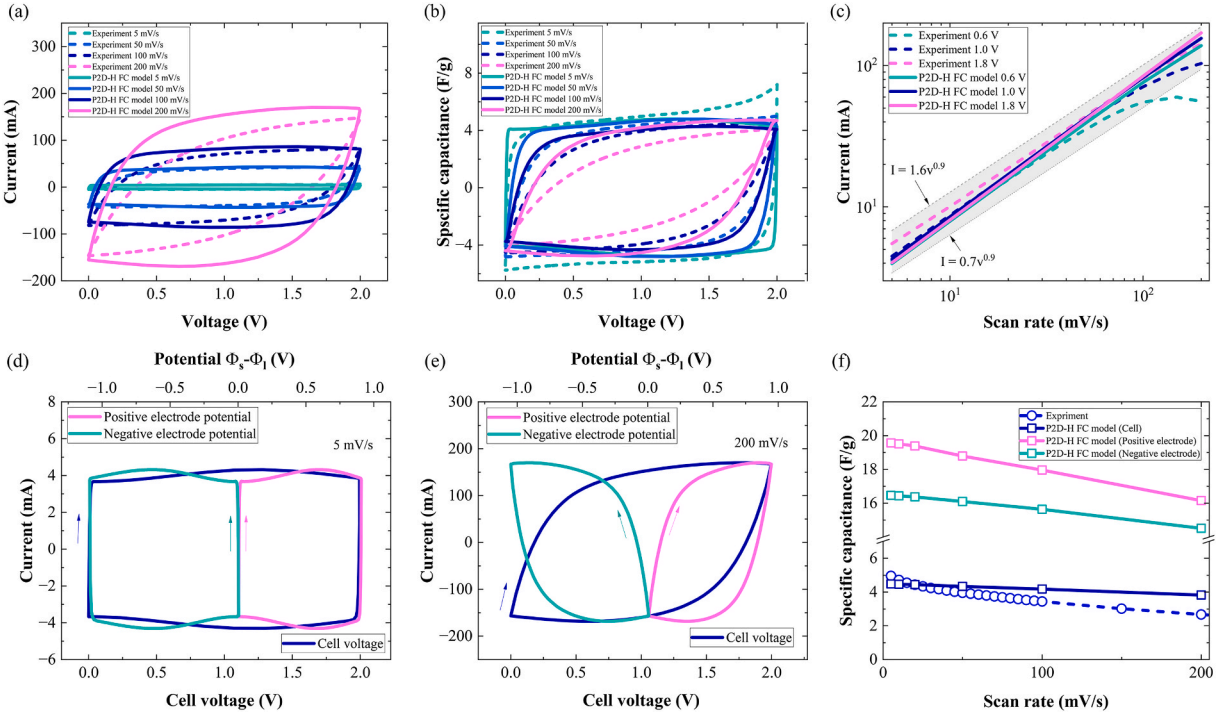

Fig. 2. (a) Cyclic voltammetry graphs and (b) specific capacitance response of a two-electrode symmetrical cell model (P2D-H FC), in comparison with the experimental data from Ref. [18]. (c) The relationship between the response current and scan rates at different cell voltages. (d)–(e) Voltammograms of positive and negative electrodes at a slow (5 mV/s) and fast (200 mV/s) scan rate predicted by the numerical model, with the resulting specific capacitance for both cell and individual electrode summarised in (f).

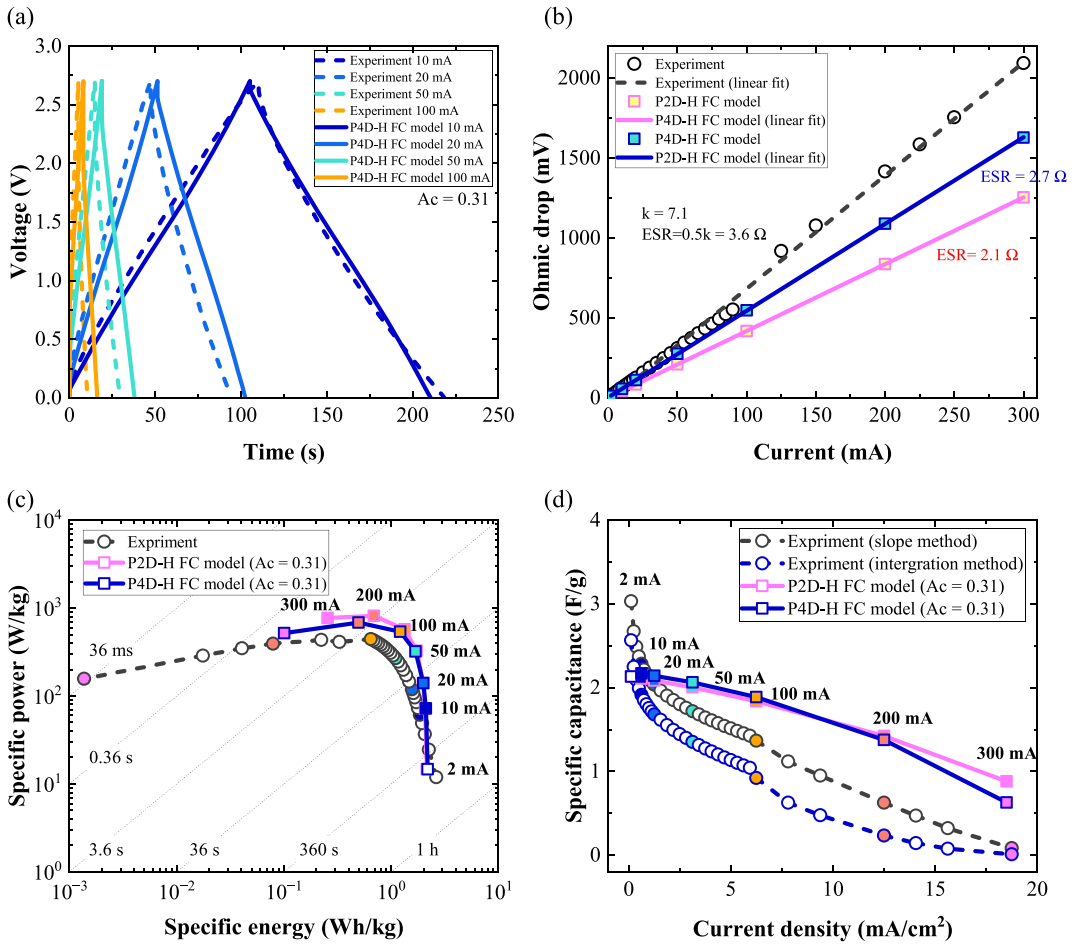

Fig. 3. (a) GCD response curves of the symmetric full cell model after the initial cycle, comparing with the experimental data from Ref. [18]. The cell performance at a charging current ranging from 2 mA to 300 mA (measured over an electrode area of 16 cm^2) was summarised, including (b) the ohmic drop at the start of the discharge which determines the ESR, (c) the specific energy and power presented in the form of a Ragone plot, and (d) the specific capacitance. A constant electrolyte accessibility A_c was assumed in the above numerical models.

performance, a rate-dependent electrolyte accessibility $A_c(i)$ was defined and calibrated from experimental data across a range of charging rates and subsequently fitted with a logarithmic function (Fig. 4c; see ESI for detailed calibration procedure). The models were then tested at a different set of charging rates (Fig. 4c), using a fitted rate-dependent $A_c(i)$. Significant improvements were achieved in the accuracy of cell performance predictions, with errors of less than 10 % in both specific energy (Fig. 4a) and specific capacitance (Fig. 4b) predictions while a consistent error of around 20 % was obtained for specific power (Fig. 4a), when the charging rate did not exceed 3.75 mA/cm^2 (60 mA/16 cm^2).

During the galvanostatic charging/discharging (Fig. 5a), when the cell reached the quasi-equilibrium state (~0.7*s* after the reverse of current direction), the electronic current density $\boldsymbol{i}_s$ presented a linear decrease/increase within the porous electrodes along the cell thickness direction from the current collector/electrode (CC/E) boundaries on both sides towards the centre, and reached zero at the electrode/separator (E/S) boundaries (Fig. 5b). The solid phase electrode potential ϕ_s increased/decreased linearly with time during constant rate charging/discharging, and was constant in the thickness direction due to the

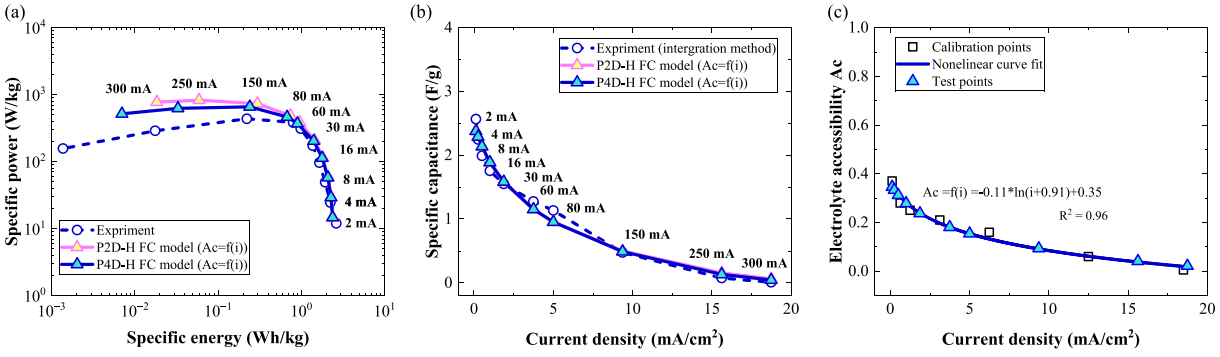

Fig. 4. The response of (b) specific energy and power, and (c) specific capacitance for symmetric full cell models using (c) calibrated rate-dependent electrolyte accessibility coefficient $A_c(i)$ during GCD at varying charging rates.

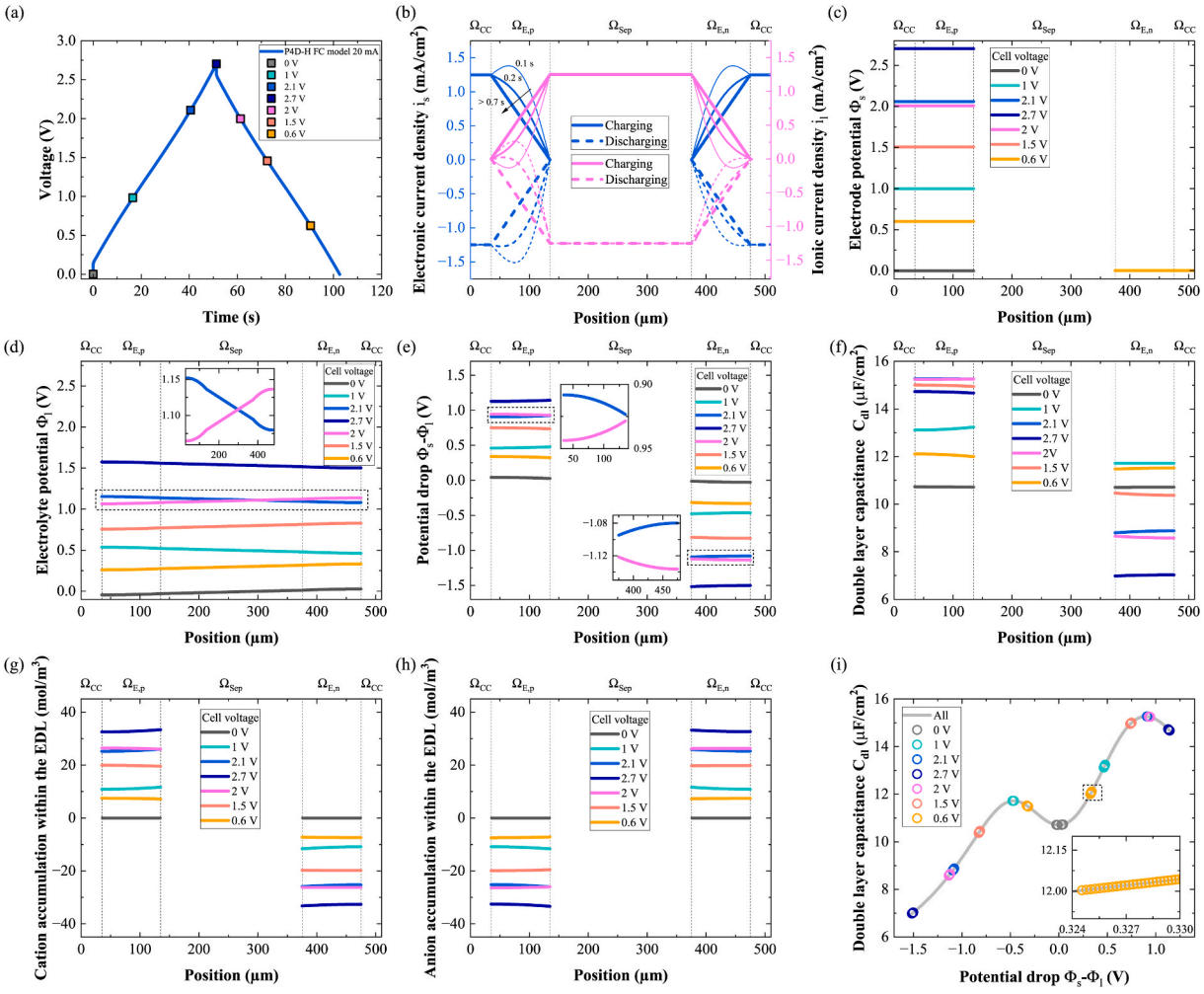

Fig. 5. (a) GCD response curve of the symmetric cell model (P2D-H FC) at a current density of 1.25 mA/cm^2 and the predicted spatial distribution of (b) electronic current density $\boldsymbol{i}_s$ and ionic current density $\boldsymbol{i}_l$ (c) solid electrode potential ϕ_s, (d) liquid electrolyte potential ϕ_l, (e) potential drop $u = \phi_s - \phi_l$, (f) differential double layer capacitance C_{dl}, (g) and (h) cation and anion concentration within the EDL along the thickness direction, as well as (i) the relationship between the double layer capacitance and the potential drop across the EDL, i.e., C_{dl}-u profile.

comparably good electrical conductivity of CAG (0.4–4.46 S/cm [48]) (Fig. 5c). To preserve a constant total current density throughout the entire cell, the ionic current density $\boldsymbol{i}_l$ along thickness direction exhibited a reverse linear distribution within the porous electrodes and kept constant within the separator domain, equal to the input current density. The overall electrolyte potential ϕ_l consistently increased over time. Spatially, it decreased in a quadratic manner within the porous electrode and linearly within the separator along the thickness direction from the positive to the negative electrode during charging, and vice versa during discharging (Fig. 5d). The resulting absolute potential drop $|u| = |\phi_s - \phi_l|$ between the solid and liquid phase of the porous electrodes presented the same quadratic increase from the CC/E boundaries to the E/S boundaries (Fig. 5e). Naturally, the same number of excess charges were stored at the EDL at each electrode to preserve the charge balance of the system (Fig. 5g and h). However, the absolute potential drop at each electrode was asymmetric, at a given cell voltage, with a larger value predicted at the negative electrode than the positive electrode (Fig. 5e). This was associated with the asymmetric voltage-dependent differential double layer capacitance C_{dl} solved by the microscale model, showing a reverse higher capacitance at the positive electrode (Fig. 5f). The relationship between the C_{dl} and the potential drop u within the whole porous electrode domain during GCD was summarised as a C_{dl}-u profile (Fig. 5i), which exhibits the signature "camel" shape for RTILs [49,50]. The C_{dl} started from the Potential of Zero Charge (PZC) and increased exponentially with $|u|$, until it reached the maxima of the humps, and then dropped with the square root of the $|u|$ at higher potentials [35].

4.3. Electrochemical impedance spectroscopy (EIS)

The Nyquist plot (Fig. 6a) generated by the numerical model displayed a 45° line starting directly from the intersection point with the real axis of the impedance at the highest frequency, followed by a 90° vertical line at lower frequencies. This profile is characteristic of porous carbon electrodes and can be effectively described using a finite-length transmission line model with a reflective boundary [51]. The 45° line region is associated with a semi-infinite linear diffusion process within the porous electrode at high frequencies. As the frequency decreases, the response transitions into a vertical line, characteristic of an ideal capacitor, due to charge saturation at the end of the impermeable pore wall. For the experimental SC device, the Nyquist plot shows a compressed semicircle directly after the ESR point, followed by a nearly linear region with slopes below 45° at intermediate frequencies. At low frequencies, the plot ends with a straight line tilted approximately 6° from the vertical.

Equivalent circuit (EC) fitting was conducted on both numerical and experimental impedance spectra to interpret the underlying mecha-

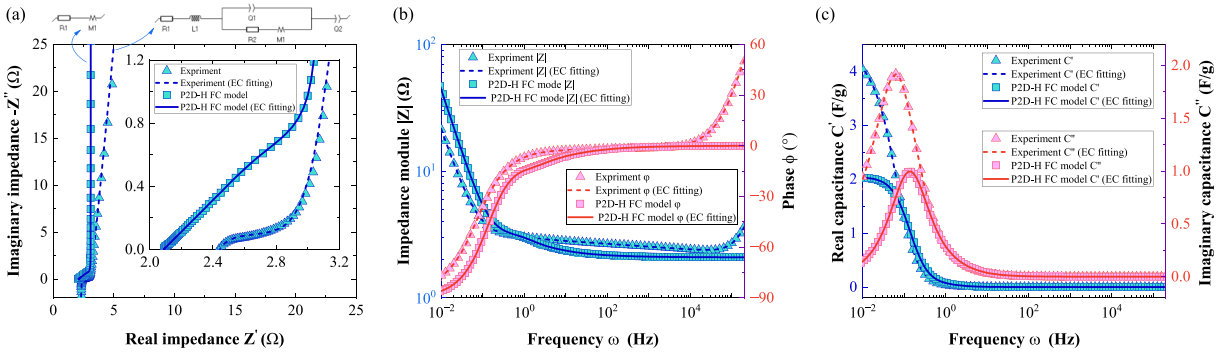

Fig. 6. The numerical and experimental [18] impedance spectrum in forms of (a) Nyquist, (b) Bode magnitude and phase angle, (c) real and imaginary capacitance plots, containing measurements over the frequency range from 10 mHz to 200 kHz, alongside the equivalent circuit fitting results.

nisms (see ESI for details). The EC for the simulation can be simply represented as a resistor R_1 for ESR in series with a restricted linear diffusion element M_1, i.e., $R_1 + M_1$. To fit the experimental impedance spectrum, a constant phase element (CPE) Q_1 was needed in parallel with a resistor R_2, along with another CPE Q_2 in series (Fig. 6a). The first component Q_1/R_2 created a flattened semicircle in the Nyquist plot at high frequencies, while the second CPE Q_2 contributed to a constant phase distortion in the 90° straight line region at low frequencies. Additionally, an inductor L_1 is included in series to account for the positive imaginary impedance at high frequencies. This configuration, $R_1 + L_1 + Q_1/(R_2 + M_1) + Q_2$, represented the entire RC circuit for a real pouch cell device.

The ESR determined from the numerical impedance spectrum was 2.1 Ω, closely aligned with the experimental value of 2.4 Ω (Fig. 6a and b). Both measurements were about 20 % lower than the ESR obtained from the GCD tests, both experimentally and numerically (Table 1). The specific capacitance predicted by the numerical model was 2.0 F/g, based on the real capacitance value at 10 mHz (Fig. 6c). This prediction was consistent with the GCD test result of 2.2 F/g (Table 1); however, it was less than half of the corresponding experimental value of 4.7 F/g at 10 mHz, The time constants derived from the frequency at maximum imaginary capacitance were in the same range, showing numerical and experimental values of 1.1 s and 2.5 s, respectively.

4.4. Homogeneous and high-fidelity model

To validate the effectiveness and accuracy of the simplified homogenous model, a GCD test at 1.25 mA/cm^2 was performed on the P4D/P2D homogenous full cell (P4D/P2D-H FC) model and the high-fidelity P4D RVE (P4D-F RVE) model with electrodes adopting single, random and aligned fibre representations with the same total equivalent fibre volume fraction V_f.

The GCD curves for all the models analysed displayed minimal differences (Fig. 7a). Although the P4D-H FC model with strip current collectors (Fig. 1b) exhibited about 30 % higher ESR (2.8 Ω) as compared to the other four models (~2.1 Ω) considered, no significant difference was observed among all models regarding the specific capacitance, specific energy and power, given their inherently low ESR values (Fig. 7b). Amongst the high-fidelity RVE models, the simulation results demonstrated that the fibre geometry and distribution can affect the path of ion flow but had a relatively minor effect on the eventual ion concentration distribution along the thickness direction (Fig. 7c). Nevertheless, the P4D-F RVE model with random fibres showed the overall longest and most tortuous ion flow path and therefore presented the highest ESR (Fig. 7b). Based on the above observation, the parametric studies described in the next Section were performed on the P2D-H FC model to save computational time.

4.5. Parametric study of constituent parameters

Separators serve to electrically isolate the porous electrodes from each other whilst permitting ion transportation between them. The separator should be as thin and porous as possible to reduce the ion transport distance and tortuosity, and to minimise parasitic weight. However, if the separator is too thin or too porous, there is an increased risk of short-circuiting due to fibre or CAG penetration. The parametric study indicated that for higher porosity ($\varepsilon_{sep} > 0.35$) separators, the cell performance was much less sensitive to the variation in separator thickness as compared to those with lower porosity ($\varepsilon_{sep} < 0.3$) (Fig. 8a–c). In the cases of higher porosity separators with thicknesses ranging from 20 to 240 μm, the cell held a consistently good performance, achieving specific power over 140 W/kg, specific energy over 2.0 Wh/kg and time constant lower than 1.6s (with electrode thickness of 100 μm and fibre volume fraction of 31 %). Alternatively, comparable cell performance can be achieved using less porous but thin-ply separators (<50 μm), which consistently outperformed their thicker counterparts (>100 μm).

The electrode thickness in the symmetric full cell model was varied from 50 μm to 200 μm, according to the typical thickness range for ultra-thin plain weave STFs, used as the basis of the structural electrodes in SSCs. A thinner electrode thickness also benefits cell performance, doubling the specific power on halving the electrode thickness from 100

Table 1
A summary of the numerical predicted and experimental measured [18] electrochemical performance of SCs with symmetric CAG-STFs electrodes in [EMIM][TFSI] electrolyte. The performance obtained from the GCD test was predicted by the P4D-H FC model with rate-dependent electrolyte accessibility. The gravimetrical performance indices were normalised by the total mass of the two electrodes.

Characterisation method	Equivalent series resistance R_{ESR} (Ω cm^2)		Maximum specific capacitance C_s (F g^{-1})			Maximum specific energy Γ_s (Wh kg^{-1}) from GCD	Maximum specific power P_s (kW kg^{-1}) from GCD	Time constant τ (s)	
	GCD	EIS	CGD	CV	EIS			CGD	EIS
Numerical	43	34	2.1	4.5	2.0	2.4	0.66	1.1	1.1
Experimental [18]	58	38	2.6	5.0	4.7	2.6	0.44	1.7	2.5

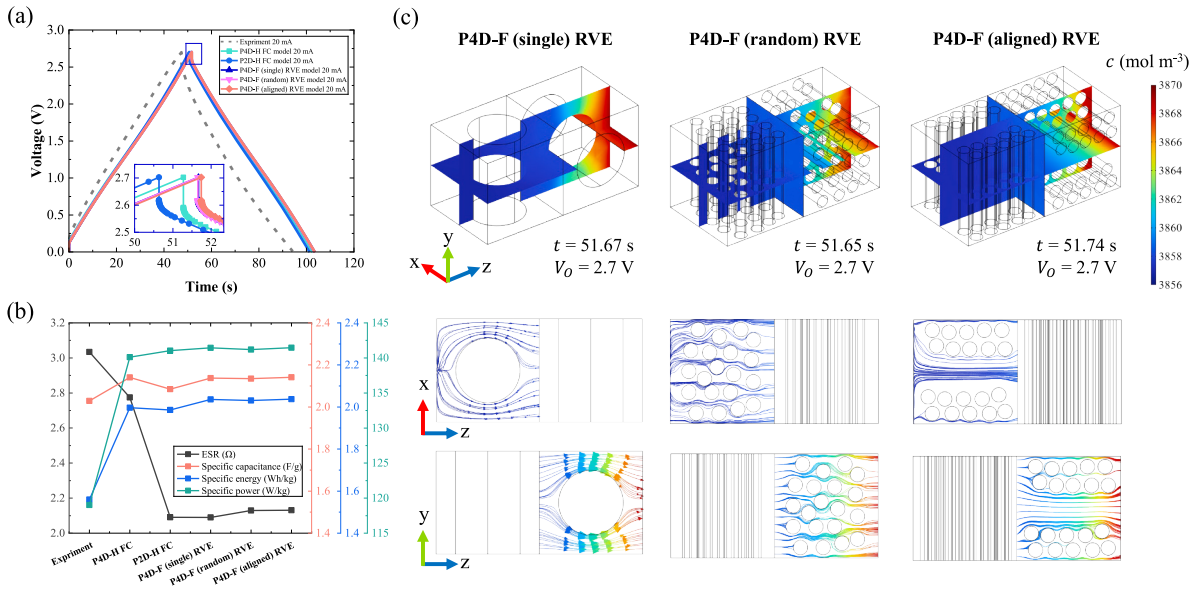

Fig. 7. Comparison of (a) GCD response curves and (b) calculated performance indices between the homogenous full cell model and high-fidelity models with different fibre representation and distribution at a current density of 1.25 mA/cm^2 (c) illustrates the ion concentration and cation flow streamlines within the positive electrode when the high-fidelity models were charged to 2.7 V.

μm to 50 μm in all fibre volume fractions (Fig. 8e); however, the improvement in specific energy was less than 2 % (Fig. 8d). On the other hand, for a given electrode thickness, the specific energy of the cell decreased rapidly as the fibre volume fraction of the electrode increased (Fig. 8d).

5. Discussion

5.1. Model accuracy and error analysis

Accurate prediction of the device performance is the prerequisite for numerical models before applying them for more advanced device design and optimisation tasks. Among the five key cell performance indicators evaluated in this study, i.e., ESR, specific capacitance, time constant, specific energy and power, the former two are more fundamental and inherent to the device materials and structure, and they determine the latter three performance indices.

The ESR accounts for the resistances of the bulk electrolyte, the electrode, and the contact resistance between the electrode and the current collector [52]. Therefore, given the accurately measured material properties input, the established physics-based continuum model can give an overall accurate prediction. Overall, the P4D-H FC model,

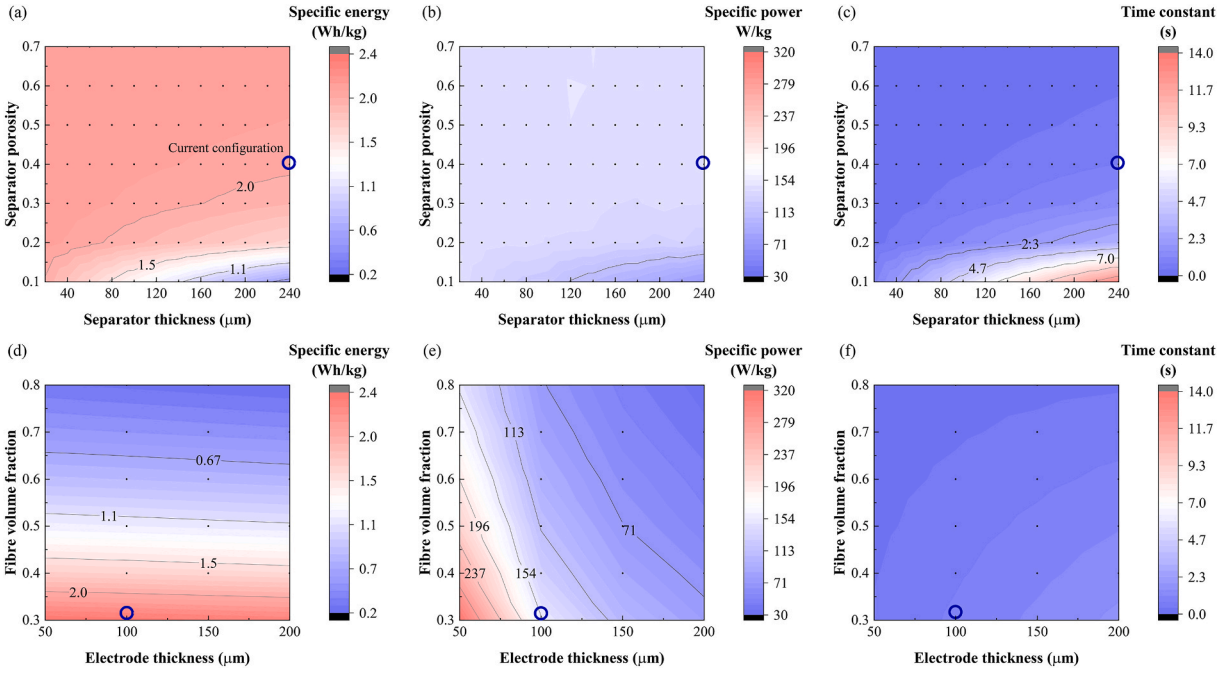

Fig. 8. Parametric study on the symmetric cell model (P2D-H FC), investigating the effects of the (a)–(c) separator thickness and separator porosity and (d)–(f) electrode thickness and fibre volume fraction on the specific energy, specific power, and time constant of the cell during GCD at a current density of 1.25 mA/cm^2.

featuring anisotropic material properties and geometric structures identical to actual devices, provided the most accurate prediction of ESR among all numerical models with different configurations considered in this study (Figs. 3b and 7b), although still presenting about 20 % underestimation. This underprediction of the ESR can steam from the uncaptured manufacturing defects in the CAG and difficulty of matching appropriate parameters to the heterogeneous system.

Due to the low overall internal resistance of the current system employing liquid electrolyte, the effects of the underpredicted ESR on the overall cell performance were small when the cell was charged at slow rates (0.125–1.875 mA/cm^2), where the differences in specific energy and specific power predicted by P4D-H FC and P2D-H FC models were less than 3 % (Figs. 3c, 4a and 7b), even though their ESRs differed by 20 %. However, as the charging rate increases, the discrepancy between the experimentally measured and predicted ohmic drop ($V_\Omega = 2R_{ESR}I_{ch}$) increase linearly (Fig. 3b), and this variation is amplified quadratically by the term V_{max}^2, thereby inducing an increasing overprediction of the specific energy ($\Gamma_s = \frac{1}{2}C_s V_{max}^2$) (Fig. 4a). Therefore, it can only be justified to use the reduced-dimension P2D FC model with isotropic material properties and fully covered CCs for cell performance estimation when the cell internal resistance was relatively low and charged at relatively slow rates. While in systems with solid electrolytes or those exhibiting significant contact resistance between the CCs and electrodes, the accuracy of the P2D model should be reevaluated.

Specific capacitance is the other crucial performance metric that determines the specific energy and is largely determined by the intrinsic double layer capacitance and electrolyte accessible SSA. In the cases where a constant electrolyte accessibility was utilised, an approximate linear reduction in the cell specific capacitance was predicted as the charging rate increased (Fig. 3d). The reduced capacitance was attributed both to the linear increase in ohmic drop (Fig. 3b) and the increasingly pronounced ion transport limitations within the electrodes (Fig. S3), where the outer region of the electrodes exhibited a lower potential drop across the EDL (Fig. S3c) and consequently lower local double layer capacitance (Fig. S3d) at high charging rates (>6.25 mA/cm^2). However, with the constant electrolyte accessibility assumption, the models cannot capture the nonlinear increase of capacitance at very slow charging rates observed in real devices, which can be associated with the enhanced accessibility of the electrolyte to micropores [53]. To address this issue, a calibrated rate-dependent $A_c(i)$ was employed instead (Fig. 4c), which was demonstrated to provide accurate predictions (<10 % error) for the specific energy and specific capacitance at slow to moderate fast charging rates (Fig. 4a and b). However, as discussed above, the underestimated ESR still induced a considerable overestimation of the specific energy and power at high charge rates (Fig. 4a). Additionally, although the $A_c(i)$ function may vary across different supercapacitor systems, the $A_c(i)$ calibrated in this study remains applicable for exploring the effects of mechanical loading/-damage on the electrochemical response of SSCs with the current material system.

5.2. Effects of constituent parameters

One of the attractions of the numerical modelling is that it allows an exploration of the materials design parameters, saving experimental resources and labour. In general, homogenisation methods have proved effective and efficient for numerical simulation of macroscopic ion transport within porous media, including porous electrodes, structural electrolytes, and separators [54,55], by assigning them with a proper effective geometrical parameter, e.g., porosity and tortuosity. While porosity is a well-defined parameter that is relatively easy to measure, quantifying tortuosity poses more challenges. Therefore, tortuosity is often derived from porosity through various functions tailored to different material types and microstructures [45,46]. The parametric study of the separator porosity (Section 4.5) was based on a modified Bruggeman relation with the cylindrical microstructure assumption for the glass fibre separator. To obtain a more accurate value of the McMullin number (ε/τ) or tortuosity as the model input parameter, experimental characterisation methods such as impedance spectroscopy [46] may be required in the future. On the other hand, the influence of thickness is consistent for different components, since a thinner layer of separator/electrode facilitates a shorter average transport path for ions to reach the pore walls of the active material, thereby promoting faster charging/discharging and enhancing the cell specific power (Fig. 8b and e). As the electrode thickness increases, diffusion limitations become more pronounced, resulting in higher internal resistance, reduced utilisation of the outer electrode regions, and lower overall energy efficiency (Fig. S4).

Increasing fibre volume fraction V_f, systematically decreases in the specific energy of CAG-STF electrodes (Fig. 8d), due to the loss of active CAG volume fraction. Since the carbon fibres have an SSA several orders of magnitude smaller than that of the CAG, they were modelled as current conductors with negligible capacitance. Additionally, since the density of the CFs is much higher than that of the CAG, the effect of the gravimetrically normalised electrochemical performance is even more significant than the relative volume fractions imply.

5.3. Surface versus diffusion-controlled kinetics

The EDL dis/charging is generally regarded as a surface-controlled non-Faradaic process [56]. In an ideal SC, the total charge stored at the electrode/electrolyte interfaces is independent of the scan rate when tested via voltammetry [57]. This response is observed for the SC models developed in this study, where the current i depends linearly depends on the applied scan rate v at a given voltage (Fig. 2c). However, the nonlinear response observed in the experimental studies indicates that real devices may exhibit kinetics that are not solely surface-controlled. To better understand the electrode kinetics involved, the i-v relationship can be fitted to the power law dependency based on the empirical equation $i = av^b$ [58,59]. If b is unity, it suggests a surface-controlled behaviour; and if it equals 0.5, the response current is proportional to the square-root of the scan rate, which is associated with the diffusion-controlled (non-capacitive, Faradaic) kinetics [57]. The fitting result of the experimental curves showed a b value between 0.86 and 0.9 in the voltage range from 0.6 to 2.0 V (Fig. 2c), suggesting a co-contribution of both surface-controlled and diffusion-controlled processes while the former still dominated (if b >0.85) [57].

These mixed kinetics were also demonstrated by the EISs (Fig. 6a), where the experimental Nyquist plot was sloped (less than 45°) and an approximately linear region at intermediate frequencies, compared with the 45° straight line at high frequencies for the numerical models under pure surface-controlled conditions. The non-vertical line with a slope less than 45° at intermediate frequencies is associated with the mixed control of ion transfer crossing the EDL and diffusion within the active material, which has been studied both experimentally [56] and numerically [52]. This impedance spectrum can be replicated by incorporating CPEs into the baseline EC model for numerical SSC models, as described in Section 4.3. One physical interpretation for the CPEs is the mixed surface-diffusion-controlled kinetics [51], consistent with the above analysis. The origin of the diffusion-controlled process could be the parasitic redox reaction of the function groups or impurities on the CAG surface [57], which can be considered in further models. Another physical interpretation for the CPE element is the interfacial impedance at the current collector/active material (CAG) interfaces [57], which could generate the semi-circle at high frequencies, as well as shift the imaginary part of the impedance at low frequencies from the theoretical 90° line (Fig. 6a).

5.4. Non-linear voltage-charge dependency

In an ideal dielectric capacitor or SC, the amount of charge stored in the cell is linearly dependent on the cell voltage, resulting in linear or triangular GCDs and rectangular CVs. The non-linear GCDs (Fig. 3a) and peak-shaped CVs (Fig. 2b) of a real SSC cell, could stem from several aspects.

The first and most fundamental factor is that the EDL is in fact not intrinsically linear, contrary to common assumptions. The differential/double-layer capacitance C_{dl} of porous carbon electrodes in IL may vary as a function of the voltage u (the potential drop across the EDL), resulting in a non-constant slope ($dV/dt = -I_{ch}/C_{dl}$) in the GCD curves. Numerous experimental studies have shown that the C_{dl}-u curve for IL on a charged planar surface is bell-shaped (as can be replicated in the Kornyshev model [35–37] with compacity factor $\gamma > 1/3$) [60] or more commonly camel-shaped ($\gamma < 1/3$) [49,50,61], rather than U-shaped in dilute electrolytes [61], due to the two competing regimes of behaviour for the EDL in ILs. At small voltages, the EDL is dominated by the ion overscreening regime induced by the electrostatic interactions between densely packed ions near the solid plane [36,38], leading an exponentially increasing C_{dl} with increasing voltage (Fig. 5i). At large voltages, ion crowding prevails over the overscreening due to the strong steric interactions of ions [36,38], resulting in a square root decay of C_{dl} with voltage. When $\gamma \to 0$, the Kornyshev model retrieves to the classic Gouy-Chapman model [35], thereby the proposed multiscale model could also be applied to diluted electrolytes, given the fact that the employed Nernst-Planck model for charge transport remains valid. However, the applicability of the Kornyshev model to moderately concentrated or concentrated aqueous/organic electrolytes remains unexplored, thereby limiting the scope of the current multiscale model.

The second source of non-linearity is more conventionally understood: the mixed surface-controlled (capacitive non-Faradaic) and diffusion-controlled (non-capacitive Faradaic) kinetics, as discussed in Section 5.3, distort the electrochemical response of a real SSC cell from the ideal SC behaviour. A third common origin of non-linear GCDs and peak-shaped CVs in supercapacitors occurs on charging beyond its maximum voltage window. Parasitic reactions, associated either with direct electrolyte decomposition or side reactions with adventitious oxygen, water, or other contaminants, reduce both the columbic efficiency and the energy efficiency [56]. Further detailed experimental studies of the maximum effective stability window for CAG electrodes in [EMIM][TFSI], operated as symmetric two-electrode devices, are underway.

5.5. Asymmetric electrode performance

An asymmetric electrochemical response of the pair of symmetric electrodes was predicted by the numerical models in both GCD (Fig. 5e and f) and CV (Fig. 2d–f) tests, with a consistently higher level of polarisation and lower capacitance at the negative electrode as compared with the positive electrode. This phenomenon has also been observed in an experimental study [49,62], which tested the operating potential window (OPW) of the same IL used in this study, i.e., [EMIM][TFSI], on pore-free onion-like carbon electrodes. This asymmetric behaviour of symmetric cells is usually attributed to mobility and size differences between anions and cations [62], although the identity of the mobile species can be complicated by the structure of the double layer at the PZC [43]. The position of the open circuit potential relative to non-linearities discussed in the previous section is also important.

During the charging/discharging of an SSC or a more general SC, the amount of charge Q stored on the two electrodes is equal (Fig. 5g and h). Given $Q = CV$, the electrode with the smaller capacitance (the negative electrode in the system studied) will require a larger polarisation to reach the charge balance. Since the electrodes were symmetric and had identical properties in the numerical models, the imbalance in the electrode capacitance stems from the asymmetric behaviour of the double layer at positive and negative polarisations (Fig. 5i). The asymmetry of the predicted capacitance-potential (C_{dl}-u) curve is associated with the ion compactness (parametrised by $\gamma(u)$) of the IL in response to the positive and negative polarisation, which are determined by the anion and cation size, as well as their excluded volumes [37]. A semi-phenomenological explanation for the effects of ion size on the double layer capacitance can be: when the cation size is substantially larger than the anion size, the maximum local concentration c_{max} of cations in the cation-rich region of the EDL is smaller than that of the anion [28,35]. Consequently, a larger ion compacity $\gamma \propto c_{bulk}/c_{max}$ will occur at the negative electrode rather than at the positive electrode, which suppresses the capacitance of the negative electrode and eventually induces larger negative polarisations than the positive polarisations. A case study in the ESI provided further support, where two other ILs, i.e., [PYR_{13}][TFSI] and [N_{1114}][TFSI], with different cation and anion capacity relationship, were tested by the P2D-H FC model. The results also revealed that a higher ion capacity led to a lower capacitance on the electrode side that adsorbed the respective ion species. Besides, this case study demonstrated that different combinations of anions and cations could impact the IL self-diffusion coefficient, double layer capacitance at PZC, as well as asymmetric behaviour at the positive and negative electrodes, subsequently influencing the overall supercapacitor cell performance.

In addition to the ion-size asymmetry in [EMIM][TFSI] (7.6 Å × 4.3 Å and 7.9 Å × 2.9 Å for cation and anion, respectively), factors such as functional groups on the electrode surface, pairing and short-range repulsions [37], as well as electrode microstructural configurations [63] and pore sizes [64] could also affect the double layer capacitance and the asymmetric behaviour of the electrodes. The porous carbon electrodes considered in this study, e.g., CAG, typically feature a hierarchical pore structure, comprising micropores, mesopores, and even macropores. Among these, micropores have been found to promote an anomalous capacitance increase for porous carbon in electrolytes with either solvated ions [65] or non-solvated ions (i.e., ILs) [64]. Moreover, the highest double layer capacitance was achieved when the pore size closely matches the ion size, enabling optimal ion packing with minimal free space [64,66]. Although the calibrated rate-dependent electrolyte accessibility somewhat reflects the increasing contribution of the micropores at slower charging rates, the established multiscale model, however, only considered an average mesopore size. This simplification represents one of the main limitations of the current model.

To improve the symmetry of the electrode response such that enhancing the cell performance, several strategies can be adopted, e.g., balancing the electrode masses, utilising different materials for the positive and negative electrode, and formulating electrolyte with mixed ILs [62]. Among these approaches, the design and optimisation process for asymmetric electrodes can be accelerated using the multiscale model proposed in this paper, which evaluates the effects of the intrinsic asymmetric behaviour of the microscale EDL at polarised electrode/electrolyte interfaces on macroscale cell performance.

6. Conclusions

In this study, a physics-based continuum multiscale electrochemical model was developed for SCs with porous carbon electrodes in an RTIL electrolyte. The proposed P4D multiscale model coupled a 3D macroscopic homogeneous model that solved the dynamical transport across the full cell, with a 1D equilibrium cylindrical mesopore EDL model, which determined the local double layer capacitance with respect to the local potential drop across the EDL solved in the macroscale model.

The multiscale model was validated by comparing the numerical and experimental results [18] of CV, GCD and EIS tests conducted on an SSC pouch cell with CAG-modified carbon fibre-reinforced electrodes in an RTIL electrolyte. An overall good accuracy was achieved in predicting various performance indices, achieving an error less than 10 % for specific energy and capacitance, and around 20 % for specific power, at

slow and moderately high charging rates ($\leq$3.75 mA/cm^2). Furthermore, the proposed multiscale model captured the effects of inherent asymmetric response of the microscale EDL during positive and negative polarisation on the macroscale cell behaviour. The model predicted an asymmetric electrochemical response of a pair of symmetric electrodes in both GCD and CV tests, where the positive electrode exhibited over 10 % higher capacitance and an inversely narrower potential window as compared with the negative electrode. Additionally, a good consistency in the cell performance prediction was achieved between the high-fidelity and homogeneous model, enabling a series of parameter studies to be conducted on the homogeneous model with low computational cost and high accuracy to determine optimal constituent parameters.

In conclusion, the multiscale model developed in this work has several potential uses: most tangibly, it provides predictions of key electrochemical performance indicators as a function of device constituents and geometry, helping to accelerate the design and optimisation of SSCs and other general SCs with porous electrodes and RTIL electrolytes. In addition, it identifies some less obvious complexities, thus shedding light on fundamental phenomena that underpin observed performance. In the longer run, a practical modelling framework may also contribute to virtual certification.

Future work will focus on enhancing the model's physical fidelity and broadening its scope of applications. Improvements may involve incorporating a realistic distribution of pore sizes or statistical pore size variability instead of relying on an average value, as well as considering ion adsorption in both micro- and mesopores to better represent the hierarchical pore structure in porous electrodes [67]. Additionally, by incorporating Faradaic processes, the model can be adapted for pseudocapacitors and hybrid ion capacitors. In the near term, efforts will focus on developing the model for a fully structural SC with a bi-continuous structural electrolyte. The modified model, especially in its high-fidelity configuration, could be employed to predict the electrochemical response of SSCs subjected to various types of mechanical damage, such as fibre breakage, CAG cracking, CF/CAG debonding, and electrode/separator delamination.

CRediT authorship contribution statement

Shimeng Qian: Writing – original draft, Visualization, Validation, Methodology, Investigation, Formal analysis, Conceptualization. **Emily Cheng:** Writing – original draft, Validation, Formal analysis. **Odysseas Kakarelidis:** Validation, Investigation, Data curation. **Sang Nguyen:** Writing – review & editing, Methodology, Investigation, Data curation, Conceptualization. **Milo.S.P. Shaffer:** Writing – review & editing, Supervision, Conceptualization. **Anthony.R.J. Kucernak:** Writing – review & editing, Supervision, Conceptualization. **Ajit Panesar:** Writing – review & editing, Supervision, Funding acquisition, Data curation, Conceptualization. **Emile S. Greenhalgh:** Writing – review & editing, Supervision, Project administration, Funding acquisition, Conceptualization.

Declaration of competing interest

The authors declare that they have no known competing interests.

Acknowledgements

The authors kindly acknowledge the funding provided by the UK Engineering and Physical Sciences Research Council (EPSRC) Programme Grant Future Composites Research Manufacturing Hub (EP/P006701/1), the EPSRC Beyond Structural project (EP/P007465/1), the European Office of Aerospace Research and Development, Realising Structural Battery Composites (IOE Grant FA8655-21-1-7040), EU Clean Sky 2 (SORCERER Project #738085) and EPSRC Realising Structural Power (EP/W03526X/1) - a collaboration between the University of Bristol, Durham university and Imperial College London. This research was also supported by the Royal Academy of Engineering under the Chairs in Emerging Technologies scheme. For the purpose of open access, the author has applied a Creative Commons Attribution (CC BY) licence to any Author Accepted Manuscript version arising.

Appendix A. Supplementary data

Supplementary data to this article can be found online at https://doi.org/10.1016/j.jpowsour.2025.238956.

Table A.1
List of abbreviations and acronyms.

Abbreviations/Acronym	Description
BET	Brunauer- Emmett-Teller
CAG	Carbon aerogel
CAG-STF	Carbon aerogel modified spread tow carbon fibre fabric
CC	Current collector
CPE	Constant phase element
CV	Cyclic voltammetry
CAG	Carbon aerogel
DC	Direct current
E	Electrode
EC	Equivalent circuit
EDL	Electric double layer
EIS	Electrochemical impedance spectroscopy
ESR	Equivalent series resistance
FC	Full cell
FE	Finite element
GCD	Galvanostatic charging and discharging
GCS	Gouy-Chapman-Stern
H	Homogenous
MPB	Modified Poisson-Boltzmann
OPW	Operating potential window
P1D/P2D/P4D	Pseudo one/two/four-dimension
PET	Porous electrode theory
RTIL	Room temperature ionic liquid

(*continued on next page*)

Table A.1 (*continued*)

Abbreviations/Acronym	Description
RVE	Representative volume element
S	Separator
SC	Supercapacitor
SPC	Structural power composites
SSA	Specific surface area
SSC	Structural supercapacitor
STF	Spread tow carbon fibre fabric
WCF	Woven carbon fibre

Table A.2
List of symbols.

Symbol	Unit	Description
α	–	Rescaling factor
Γ_s	J kg^{-1}	Specific energy
γ	–	Ion compacity
ε_m	–	Porosity
$\boldsymbol{\sigma}_s$	S m^{-1}	Electrode conductivity tensor
σ_l^{eff}	S m^{-1}	Effective electrolyte conductivity
τ_m	–	Tortuosity
τ	s	Time constant
ϕ_s	V	Solid phase potential
ϕ_l	V	Liquid phase potential
Ω	–	Domain
$\partial\Omega$	–	Boundary
A_c	–	Electrolyte-accessibility
a_s	m^2 m^{-3}	Specific surface area of the electrode
a_c	m^2 m^{-3}	Electrolyte accessible specific surface area
a	m	Ion size
c	mol m^{-3}	Molar concentration
C_{dl}	F m^{-2}	Differential/double layer capacitance
$\widetilde{C_0}$	F m^{-2}	Debye capacitance
D^{eff}	m^2 s^{-1}	Effective diffusion coefficient
d	m	Distance between the pore wall and the centre of the ion
F	C mol^{-1}	Faraday's constant
f	Hz	Frequency
$\boldsymbol{i}_s$	A m^{-2}	Electronic current density vector
$\boldsymbol{i}_l$	A m^{-2}	Ionic current density vector
i_{dl}	A m^{-3}	Double layer current density
j_{dl}	mol m^{-2} s^{-1}	Double layer flux density
$\boldsymbol{N}$	mol m^{-2} s^{-1}	Mass flux density vector
P_s	W kg^{-1}	Specific power
q	C	Charge
R	J K^{-1} mol^{-1}	Universal gas constant
R_p	m	Average pore radius
T	K	Temperature
t	s	Time
t_m	m	Thickness
u	–	Dimensionless voltage normalised by thermal voltage
V	V	Cell voltage
V_O	V	Operating cell voltage
V_{max}	V	Maximum cell discharging voltage
V_{min}	V	Minimum cell discharging voltage
V_f	–	Fibre volume fraction
$\boldsymbol{v}$	m s^{-1}	Velocity vector
ν	V s^{-1}	Scan rate
$\boldsymbol{x}$	m	Spatial position vector
z_i	–	Valence number of species i

Table A.3
List of input parameters for the electrochemical model of the SSC cell.

Parameters	Symbol	Value	Unit	Description
Physics constants				
Faraday's constant	F	96485.3	C mol^{-1}	
Universal gas constant	R	8.314	J K^{-1} mol^{-1}	
Temperature	T	298	K	
Electrode properties				
Electrode thickness	t_{ele}	100	μm	CAG-STFs
Fibre volume fraction	V_f	0.308	–	CAG-STFs
Electrode porosity	ϵ_{ele}	0.205 [18]	–	CAG-STFs
		0.296	–	CAG
Specific surface area (SSA)	a_s	1.38×10^8 [18]	m^2 m^{-3}	CAG-STFs (BET)
		2.00×10^8 [18]	m^2 m^{-3}	CAG (BET)
Electrolyte-accessibility coefficient	A_c	0.31	–	
Electrode conductivity	σ_s	1.45×10^4 [68]	S m^{-1}	CAG-STFs, in-plane
		580 [68]	S m^{-1}	CAG-STFs, out-of-plane
		446 [48]	S m^{-1}	CAG, isotropic
		7.69×10^4	S m^{-1}	Carbon fibre, longitudinal
		1.54×10^4 [69]	S m^{-1}	Carbon fibre, transverse
Electrode tortuosity	$\tau_{ele} = 2\epsilon_{ele}{}^{-1/2}$	4.41	–	CAG-STFs
		1.78	–	CAG
Average pore radius	R_p	1.9×10^{-9}	m	CAG
Separator properties				
Separator thickness	t_{sep}	2.4×10^{-4} [18]	m	Non-woven GFs
Separator porosity	ϵ_{sep}	0.40	–	Non-woven GFs
Separator tortuosity	$\tau_{sep} = 2\epsilon_{sep}{}^{-1}$	5.0	–	Non-woven GFs
Electrolyte properties				[EMIM][TFSI]
Bulk IL concentration	c_{bulk}	3884.4	mol m^{-3}	
Bulk diffusion coefficient of cation	D_+^{bulk}	3.60×10^{-11} [70]	m^2 s^{-1}	
Bulk diffusion coefficient of anion	D_-^{bulk}	2.45×10^{-11} [70]	m^2 s^{-1}	
Cation size	a_+	0.76 [64]	nm	
Anion size	a_-	0.79 [64]	nm	
EDL parameters				
Debye capacitance	$\widetilde{C_0}$	0.12 [49]	F m^{-2}	
Rescaling factor	α	0.112 [49]	–	
Cation fraction	γ_+	0.26 [49]	–	
Anion fraction	γ_-	0.087 [49]	–	
Current collector properties				
Electrical conductivity	$\sigma_{cc,in}$	1×10^5 [71]	S m^{-1}	Graphite
	$\sigma_{cc,out}$	500 [71]	S m^{-1}	Graphite

Data availability

All underlying data to support the conclusions are provided within the manuscript and supplementary information.

References

[1] F. Wang, X. Wu, X. Yuan, Z. Liu, Y. Zhang, L. Fu, Y. Zhu, Q. Zhou, Y. Wu, W. Huang, Latest advances in supercapacitors: from new electrode materials to novel device designs, Chem. Soc. Rev. 46 (22) (2017) 6816–6854.

[2] Poonam, K. Sharma, A. Arora, S.K. Tripathi, Review of supercapacitors: materials and devices, J. Energy Storage 21 (2019) 801–825.

[3] J. Zhao, A.F. Burke, Review on supercapacitors: technologies and performance evaluation, J. Energy Chem. 59 (2021) 276–291.

[4] M. Şahin, F. Blaabjerg, A. Sangwongwanich, A comprehensive review on supercapacitor applications and developments, Energies 15 (3) (2022).

[5] E.S. Greenhalgh, S. Nguyen, M. Valkova, N. Shirshova, M.S.P. Shaffer, A.R. J. Kucernak, A critical review of structural supercapacitors and outlook on future research challenges, Compos. Sci. Technol. 235 (2023).

[6] S. Nguyen, D.B. Anthony, T. Katafiasz, G. Qi, S. Razavi, E. Senokos, E. S. Greenhalgh, M.S.P. Shaffer, A.R.J. Kucernak, P. Linde, Manufacture and characterisation of a structural supercapacitor demonstrator, Compos. Sci. Technol. 245 (2024).

[7] M.F. Pernice, G. Qi, E. Senokos, D.B. Anthony, S. Nguyen, M. Valkova, E. S. Greenhalgh, M.S.P. Shaffer, A.R.J. Kucernak, Mechanical, electrochemical and multifunctional performance of a CFRP/carbon aerogel structural supercapacitor and its corresponding monofunctional equivalents, Multifunction. Mater. 5 (2) (2022).

[8] F. Danzi, R.M. Salgado, J.E. Oliveira, A. Arteiro, P.P. Camanho, M.H. Braga, Structural batteries: a review, Molecules 26 (8) (2021).

[9] N. Shirshova, T. Rogaume, H. Najmi, M. Poisson, The combustion behavior of epoxy-based multifunctional electrolytes, Fire Mater. 46 (1) (2021) 192–204.

[10] L.M. Schneider, A. Riazanova, D. Zenkert, G. Lindbergh, Effect of electrolyte composition on biphasic structural electrolytes for laminated structural batteries, ACS Appl. Energy Mater. 7 (19) (2024) 8838–8850.

[11] H.v. Helmholtz, Ueber einige Gesetze der Vertheilung elektrischer Ströme in körperlichen Leitern, mit Anwendung auf die thierisch-elektrischen Versuche (Schluss.), Ann. Phys. 165 (7) (1853) 353–377.

[12] L. Pilon, H. Wang, A. d'Entremont, Recent advances in continuum modeling of interfacial and transport phenomena in electric double layer capacitors, J. Electrochem. Soc. 162 (5) (2015) A5158–A5178.

[13] J. Snyder, E. Gienger, E. Wetzel, Performance metrics for structural composites with electrochemical multifunctionality, J. Compos. Mater. 49 (15) (2015) 1835–1848.

[14] H. Qian, H. Diao, N. Shirshova, E.S. Greenhalgh, J.G. Steinke, M.S. Shaffer, A. Bismarck, Activation of structural carbon fibres for potential applications in multifunctional structural supercapacitors, J. Colloid Interface Sci. 395 (2013) 241–248.

[15] N. Shirshova, H. Qian, M. Houlle, J.H. Steinke, A.R. Kucernak, Q.P. Fontana, E. S. Greenhalgh, A. Bismarck, M.S. Shaffer, Multifunctional structural energy storage composite supercapacitors, Faraday Discuss 172 (2014) 81–103.

[16] W. Chen, R.B. Rakhi, M.N. Hedhili, H.N. Alshareef, Shape-controlled porous nanocarbons for high performance supercapacitors, J. Mater. Chem. A 2 (15) (2014).

[17] A. Javaid, M.B. Zafrullah, F.u.H. Khan, G.M. Bhatti, Improving the multifunctionality of structural supercapacitors by interleaving graphene nanoplatelets between carbon fibers and solid polymer electrolyte, J. Compos. Mater. 53 (10) (2019) 1401–1409.

[18] H.D. Asfaw, A. Kucernak, E.S. Greenhalgh, M.S.P. Shaffer, Electrochemical performance of supercapacitor electrodes based on carbon aerogel-reinforced spread tow carbon fiber fabrics, Compos. Sci. Technol. 238 (2023).
[19] M. Valkova, D.B. Anthony, A.R.J. Kucernak, M.S.P. Shaffer, E.S. Greenhalgh, Predicting the mechanical behaviour of structural supercapacitor composites, Compos. Appl. Sci. Manuf. 156 (2022).
[20] S.P. Ong, O. Andreussi, Y. Wu, N. Marzari, G. Ceder, Electrochemical windows of room-temperature ionic liquids from molecular dynamics and density functional theory calculations, Chem. Mater. 23 (11) (2011) 2979–2986.
[21] P.M. Biesheuvel, M.Z. Bazant, Nonlinear dynamics of capacitive charging and desalination by porous electrodes, Phys. Rev. E - Stat. Nonlinear Soft Matter Phys. 81 (3 Pt 1) (2010) 031502.
[22] D. Boonpakdee, C.F. Guajardo Yévenes, W. Surareungchai, C. La-o-vorakiat, Exploring non-linearities of carbon-based microsupercapacitors from an equivalent circuit perspective, J. Mater. Chem. A 6 (16) (2018) 7162–7167.
[23] L.E. Helseth, Comparison of methods for finding the capacitance of a supercapacitor, J. Energy Storage 35 (2021).
[24] M.W. Verbrugge, P. Liu, Microstructural analysis and mathematical modeling of electric double-layer supercapacitors, J. Electrochem. Soc. 152 (5) (2005) D79.
[25] S. Allu, B. Velamur Asokan, W.A. Shelton, B. Philip, S. Pannala, A generalized multi-dimensional mathematical model for charging and discharging processes in a supercapacitor, J. Power Sources 256 (2014) 369–382.
[26] Y. Wang, C. Zhang, X. Qiao, A.N. Mansour, X. Zhou, Three-dimensional modeling of mediator-enhanced solid-state supercapacitors, J. Power Sources 423 (2019) 18–25.
[27] John Newman, K.E. Thomas-Alyea, Electrochemical Systems, John Wiley & Sons, 2004.
[28] M.V. Fedorov, A.A. Kornyshev, Ionic liquids at electrified interfaces, Chem. Rev. 114 (5) (2014) 2978–3036.
[29] G. Gouy, In the constitution of the electric charge on the surface of an electrolyte [Sur la constitution de la charge électrique ala surface d'un électrolyte], Compt. Rend 149 (1909) 654–657.
[30] D.L. Chapman, LI. A contribution to the theory of electrocapillarity, London, Edinburgh Dublin Phil. Mag. J. Sci. 25 (148) (1913) 475–481.
[31] O. Stern, Zur theorie der elektrolytischen doppelschicht, Zeitschrift für Elektrochemie und angewandte physikalische Chemie 30 (21-22) (1924) 508–516.
[32] M.Z. Bazant, M.S. Kilic, B.D. Storey, A. Ajdari, Towards an understanding of induced-charge electrokinetics at large applied voltages in concentrated solutions, Adv. Colloid Interface Sci. 152 (1–2) (2009) 48–88.
[33] J. Bikerman, XXXIX. Structure and capacity of electrical double layer, London, Edinburgh Dublin Phil. Mag. J. Sci. 33 (220) (1942) 384–397.
[34] J. Wu, Understanding the electric double-layer structure, capacitance, and charging dynamics, Chem. Rev. 122 (12) (2022) 10821–10859.
[35] A.A. Kornyshev, Double-Layer in Ionic Liquids: Paradigm Change? ACS Publications, 2007, pp. 5545–5557.
[36] M.Z. Bazant, B.D. Storey, A.A. Kornyshev, Double layer in ionic liquids: overscreening versus crowding, Phys. Rev. Lett. 106 (4) (2011) 046102.
[37] Z.A.H. Goodwin, G. Feng, A.A. Kornyshev, Mean-field theory of electrical double layer in ionic liquids with account of short-range correlations, Electrochim. Acta 225 (2017) 190–197.
[38] Z.A.H. Goodwin, J.P. de Souza, M.Z. Bazant, A.A. Kornyshev, Mean-Field Theory of the Electrical Double Layer in Ionic Liquids, Encyclopedia of Ionic Liquids, 2021, pp. 1–13.
[39] J. Huang, B.G. Sumpter, V. Meunier, A universal model for nanoporous carbon supercapacitors applicable to diverse pore regimes, carbon materials, and electrolytes, Chemistry 14 (22) (2008) 6614–6626.
[40] J.F. Gabitto, C. Tsouris, A review of transport models in charged porous electrodes, Front. Chem. Eng. 4 (2023).
[41] P.M. Biesheuvel, Y. Fu, M.Z. Bazant, Diffuse charge and Faradaic reactions in porous electrodes, Phys. Rev. E - Stat. Nonlinear Soft Matter Phys. 83 (6 Pt 1) (2011) 061507.
[42] M. Kroupa, G.J. Offer, J. Kosek, Modelling of supercapacitors: factors influencing performance, J. Electrochem. Soc. 163 (10) (2016) A2475–A2487.
[43] J.M. Griffin, A.C. Forse, W.Y. Tsai, P.L. Taberna, P. Simon, C.P. Grey, In situ NMR and electrochemical quartz crystal microbalance techniques reveal the structure of the electrical double layer in supercapacitors, Nat. Mater. 14 (8) (2015) 812–819.
[44] G.W. Richardson, J.M. Foster, R. Ranom, C.P. Please, A.M. Ramos, Charge transport modelling of Lithium-ion batteries, Eur. J. Appl. Math. 33 (6) (2021) 983–1031.
[45] B. Tjaden, S.J. Cooper, D.J.L. Brett, D. Kramer, P.R. Shearing, On the origin and application of the Bruggeman correlation for analysing transport phenomena in electrochemical systems, Curr. Opin. Chem. Eng. 12 (2016) 44–51.
[46] J. Landesfeind, J. Hattendorff, A. Ehrl, W.A. Wall, H.A. Gasteiger, Tortuosity determination of battery electrodes and separators by Impedance Spectroscopy, J. Electrochem. Soc. 163 (7) (2016) A1373–A1387.
[47] E.S. Greenhalgh, S. Nguyen, L.E. Asp, A. Bici, A. Bismarck, D. Fam, M. Johansson, G. Lindbergh, J.L. Lutkenhaus, M.S.P. Shaffer, N. Shirshova, M. Srinivasan, J. Xu, D. Zenkert, Characterization and reporting protocols for structural power composites: a perspective, Adv. Energy Mater. 15 (42) (2025) e04702.
[48] A.N. Malkova, N.A. Sipyagina, I.O. Gozhikova, Y.A. Dobrovolsky, D.V. Konev, A. E. Baranchikov, O.S. Ivanova, A.E. Ukshe, S.A. Lermontov, Electrochemical properties of carbon aerogel electrodes: dependence on synthesis temperature, Molecules 24 (21) (2019).
[49] J.M. Klein, E. Panichi, B. Gurkan, Potential dependent capacitance of [EMIM][TFSI], [N(1114)][TFSI] and [PYR(13)][TFSI] ionic liquids on glassy carbon, Phys. Chem. Chem. Phys. 21 (7) (2019) 3712–3720.
[50] M. Jitvisate, J.R.T. Seddon, Direct measurement of the differential capacitance of solvent-free and dilute ionic liquids, J. Phys. Chem. Lett. 9 (1) (2018) 126–131.
[51] A.C. Lazanas, M.I. Prodromidis, Electrochemical impedance Spectroscopy-A tutorial, ACS Meas. Sci. Au 3 (3) (2023) 162–193.
[52] B.-A. Mei, O. Munteshari, J. Lau, B. Dunn, L. Pilon, Physical interpretations of nyquist plots for EDLC electrodes and devices, J. Phys. Chem. C 122 (1) (2017) 194–206.
[53] Y. Gao, Y.S. Zhou, M. Qian, X.N. He, J. Redepenning, P. Goodman, H.M. Li, L. Jiang, Y.F. Lu, Chemical activation of carbon nano-onions for high-rate supercapacitor electrodes, Carbon 51 (2013) 52–58.
[54] V. Tu, F. Larsson, K. Runesson, R. Jänicke, Variationally consistent homogenization of electrochemical ion transport in a porous structural battery electrolyte, Eur. J. Mech. Solid. 98 (2023).
[55] M. Zhuo, D. Grazioli, A. Simone, Tensorial effective transport properties of Li-ion battery separators elucidated by computational multiscale modeling, Electrochim. Acta 393 (2021).
[56] G.Z. Chen, Linear and non-linear pseudocapacitances with or without diffusion control, Prog. Nat. Sci. Mater. Int. 31 (6) (2021) 792–800.
[57] T.S. Mathis, N. Kurra, X. Wang, D. Pinto, P. Simon, Y. Gogotsi, Energy storage data reporting in perspective—guidelines for interpreting the performance of electrochemical energy storage systems, Adv. Energy Mater. 9 (39) (2019).
[58] H. Lindström, S. Södergren, A. Solbrand, H. Rensmo, J. Hjelm, A. Hagfeldt, S.-E. Lindquist, Li+ ion insertion in TiO2 (anatase). 2. Voltammetry on nanoporous films, J. Phys. Chem. B 101 (39) (1997) 7717–7722.
[59] A. Cymann-Sachajdak, M. Graczyk-Zajac, G. Trykowski, M. Wilamowska-Zawłocka, Understanding the capacitance of thin composite films based on conducting polymer and carbon nanostructures in aqueous electrolytes, Electrochim. Acta 383 (2021).
[60] N. Nishi, S. Yasui, A. Hashimoto, T. Sakka, Anion dependence of camel-shape capacitance at the interface between mercury and ionic liquids studied using pendant drop method, J. Electroanal. Chem. 789 (2017) 108–113.
[61] M.M. Islam, M.T. Alam, T. Ohsaka, Electrical double-layer structure in ionic liquids: a corroboration of the theoretical model by experimental results, J. Phys. Chem. C 112 (42) (2008) 16568–16574.
[62] K.L. Van Aken, M. Beidaghi, Y. Gogotsi, Formulation of ionic-liquid electrolyte to expand the voltage window of supercapacitors, Angew Chem. Int. Ed. Engl. 54 (16) (2015) 4806–4809.
[63] P.F.R. Ortega, G.A.d. Santos, J.P.C. Trigueiro, G.G. Silva, N. Quintanal, C. Blanco, R.L. Lavall, R. Santamaría, Insights on the behavior of imidazolium ionic liquids as electrolytes in carbon-based supercapacitors: an applied electrochemical approach, J. Phys. Chem. C 124 (29) (2020) 15818–15830.
[64] C. Largeot, C. Portet, J. Chmiola, P.-L. Taberna, Y. Gogotsi, P. Simon, Relation between the ion size and pore size for an electric double-layer capacitor, J. Am. Chem. Soc. 130 (9) (2008) 2730–2731.
[65] J. Chmiola, G. Yushin, Y. Gogotsi, C. Portet, P. Simon, P.-L. Taberna, Anomalous increase in carbon capacitance at pore sizes less than 1 nanometer, Science 313 (5794) (2006) 1760–1763.
[66] X. Wang, H. Zhou, E. Sheridan, J.C. Walmsley, D. Ren, D. Chen, Geometrically confined favourable ion packing for high gravimetric capacitance in carbon–ionic liquid supercapacitors, Energy Environ. Sci. 9 (1) (2016) 232–239.
[67] G. Dai, L. Zhang, Y. Liao, Y. Shi, J. Xie, F. Lei, L. Fan, Multi-Scale model for describing the effect of pore structure on carbon-based electric double layer, J. Phys. Chem. C 124 (7) (2020) 3952–3961.
[68] S. Qian, S. Nguyen, A. Panesar, M.S.P. Shaffer, E.S. Greenhalgh, The electrical response of carbon fibre reinforced electrodes in structural power composites under cyclic compaction, Compos. Sci. Technol. 261 (2025).
[69] X. Ji, S. Matsuo, N.R. Sottos, D.G. Cahill, Anisotropic thermal and electrical conductivities of individual polyacrylonitrile-based carbon fibers, Carbon 197 (2022) 1–9.
[70] M.Y. Yang, B.V. Merinov, S.V. Zybin, W.A. Goddard, E.K. Mok, H.J. Hah, H.E. Han, Y.C. Choi, S.H. Kim, Transport properties of imidazolium based ionic liquid electrolytes from molecular dynamics simulations, Electrochem. Sci. Adv. 2 (2) (2021).
[71] M. Cermak, N. Perez, M. Collins, M. Bahrami, Material properties and structure of natural graphite sheet, Sci. Rep. 10 (1) (2020) 18672.